Mechanical Studies of Bovine Serum Albumin-based Bioplastics in Additive Manufacturing

Meijing Zhang

A thesis

submitted in partial fulfillment of the

requirements for the degree of

Master of Science in Applied Chemical Science and Technology

University of Washington

2025

Committee:

Alshakim Nelson

Matthew R. Golder

Program Authorized to Offer Degree:

Chemistry

University of Washington

Abstract

Mechanical Studies of Bovine Serum Albumin-based Bioplastics in Additive Manufacturing

Meijing Zhang

Chair of the Supervisory Committee:

Alshakim Nelson

Department of Chemistry

Additive manufacturing (AM), or 3D printing, has revolutionized material fabrication by enabling customization, low-cost prototyping, and high efficiency. Vat photopolymerization, a widely used AM technique, uses light to selectively cure resins, offering high resolution and fast printing speed. However, most commercial resins are petroleum-based, exhibiting low biocompatibility and degradability, which limits their use in biomedical sustainability applications. This study investigates the mechanical properties of bovine serum albumin (BSA)-based bioplastics and methods to enhance the mechanical performance of BSA-based bioplastics. BSA-based bioplastics offer tunable mechanical properties that are comparable to commercial products. A dataset of 152 commercial resins from eight leading 3D printing companies was analyzed to create Ashby plots — in many cases, BSA-based bioplastics outperformed commercial resins in both strength and ductility while offering greater biodegradability. To further enhance the mechanical performance of these bioplastics, tannic acid (TA) and heat treatments were applied to methacrylated BSA (MA-BSA) materials. Swelling in TA followed by a denaturing thermal cure on printed structure was found to enhance the non-covalent bonding within the network

and reduce rehydration, which increased Young's modulus from 389 MPa to 757 MPa and improved ultimate tensile strength fivefold. With additional solvent exchange with ethanol, the Young's modulus of MA-BSA bioplastics rose to 1.3 GPa, which made it comparable to those commercial bio-based resins. These advancements showcase BSA-based bioplastics as a promising, sustainable alternative for future biomedical 3D printing applications

Table of Contents

List of Figures 3

List of Tables 6

Chapter 1. Introduction 7

1.1. Introduction to Additive Manufacturing 7

1.2. Vat Photopolymerization 8

1.3. Protein-based Materials 10

1.4. Objective of Thesis 13

Chapter 2. Background and Comparison of Commercial Resins and BSA-Based Materials 15

2.1. 3D Printing Market Overview 15

2.2. Ashby Plots for Material Selection 16

2.2.1. Stress-strain Curve 18

2.3. Trends and Observations 19

2.4. Background on BSA-based Materials in Nelson Lab 20

2.4.1. Methacrylated BSA (MA-BSA)[50,51] 20

2.4.2. BSA/PEG-DA Bioplastics[52] 22

2.4.5. NB-BSA Double Network Bioplastics 25

2.5. Comparative Analysis Between BSA-based Materials and Commercial Resins 26

Chapter 3. Optimized Processing Methods for MA-BSA-based Bioplastics 28

3.1. Materials and Experimental Methods 28
3.1.1. Materials 28
3.1.2. MA-BSA Synthesis 29
3.1.3. Dynamic Light Scattering (DLS) 29
3.1.4. Liquid Chromatography Tandem Mass Spectrometry (LC-MS/MS) 29
3.1.5. Resin Preparation Protocol 30
3.1.6. 3D Printing Parameters 30
3.1.7. Mechanical Testing of MA-BSA/PEG-DA Bioplastics 31
3.1.8. Attenuated Total Reflection Fourier Transform Infrared (ATR-FTIR) Spectroscopy .. 32
3.1.9. Swelling Ratio of MA-BSA/PEG-DA Bioplastics 32
3.2. Results and Discussion 32
3.2.1 MA-BSA Characterization by Dynamic Light Scattering 32
3.2.2. MA-BSA Functionalization by Mass Spectrometry 34
3.2.3. 3D Printing 36
3.2.4. Tensile Testing 39
3.2.5. Swelling Ratios 46
3.2.6. Future Work on Biocompatibility 47
3.3. Conclusion 48
3.4. References 48

List of Figures

Figure 1.1. Workflow of additive manufacturing. A Computer-Aided Design (CAD) file is first designed and sliced into printable layers. After the part is printed layer by layer, some post-print processing methods are employed to have the desirable mechanical properties.

Figure 1.2. Graphical representations of material extrusion (left) and vat photopolymerization (right) and their key features.

Figure 1.3. Schematic representation of a sustainable additive manufacturing cycle. Renewable feedstocks serve as the primary materials for 3D printing. After use, the printed parts can be reused, recycled, or biodegradable for closed-loop sustainability.

Figure 2.1. An example of an Ashby plot that illustrates the relationship between Young's modulus and density across a range of material classes, including metals, polymers, foams, natural materials, and composites.

Figure 2.2. Stress–strain curve illustrating the mechanical behavior of a plastic material. Slope of the linear elastic region defines Young's modulus. After reaching the yield point, irreversible plastic deformation begins and necking until the material ultimately breaks apart. Toughness is calculated to be the area under stress-strain curve.

Figure 2.3. (a) Pie chart for the distribution of material types—rigid plastics (65.7%), semi-rigid plastics (14.1%), and elastomers (20.2%) — within the compiled mechanical property dataset from this study. (b) An Ashby plot comparing tensile strength and strain of commercial resins. (c) An Ashby plot comparing tensile strength and Young's modulus of commercial resins.

Figure 2.4. (a) Schematic showing the steps of preparing MA-BSA/PEG-DA resin from methacrylation and radical polymerization. (b) Ashby plot comparing tensile strength and strain at break for MA-BSA-based hydrogels against commercial resin categories.

Figure 2.5. (a) Schematic showing the BSA/PEG-DA resin from Michael addition and network formation. (b) Ashby plot comparing tensile strength and strain at break for BSA/PEG-DA bioplastics with various concentrations of glycerol or hyperbranched poly(glycerol)s as additives against commercial resin categories.

Figure 2.6. (a) Schematic showing the NB-BSA/PEG-2SH thiolene chemistry to form polymer network. (b) Ashby plot comparing tensile strength and strain at break for NB-BSA/PEG-2SH bioplastics against commercial resin categories.

Figure 2.7. (a) Schematic showing the formation of NB-BSA double network. (b) Ashby plot comparing tensile strength and strain at break for NB-BSA double network bioplastics against commercial resin categories.

Figure 2.8. Ashby plot comparing tensile strength and strain at break for BSA-based bioplastics against commercial resin categories.

Figure 3.1. A schematic workflow of MA-BSA/PEG-DA bioplastics sample preparation.

Figure 3.2. Dynamic light scattering spectrum showing the particle size distribution of pure BSA and synthesized MA-BSA.

Figure 3.3. Mass spectrum of (a) BSA and (b) synthesized MA-BSA.

Figure 3.4. Microscopic images of printed structures with various holes and voids evaluated at three exposure times (8 s, 9 s, and 10 s). Three viewing angles were monitored to assess dimensional fidelity and resolution. CAD models are shown in the leftmost column for comparison with the actual printed results.

Figure 3.5. Microscopic images of MA-BSA/PEG-DA bioplastic structures printed with an exposure time of 10 seconds. The printed samples were imaged after 24 hours of air drying.

Figure 3.6. Resolution test for MA-BSA/PEG-DA materials printed with line widths of 1000, 500, 250, and 100 μm. The left image shows the microscopic view of the printed sample, while the right image displays the corresponding CAD design.

Figure 3.7. Representative tensile stress-strain curves of MA-BSA/2-HEA bioplastics after 24-hours swelling in DI water. Four different procedures were tested to optimize and reproduce the mechanical properties that have been reported.

Figure 3.8. (a) Representative tensile stress-strain curves of MA-BSA/PEG-DA bioplastics with optimized processing methods as TA and heat treatments. Bar plots used to compare (b) Young's modulus (c) ultimate tensile strength, and (d) toughness between MA-BSA/PEG-DA hydrogels and bioplastics.

Figure 3.9. ATR-FTIR spectra of MA-BSA/PEG-DA with and without heat treatment. The beta-sheet peak formations are indicators of the heat-induced protein denaturation.

Figure 3.10. (a) Representative stress-strain curves of MA-BSA/PEG-DA bioplastics after solvent exchange and subsequent TA and/or heat treatment. (b) Bar plots used to compare the Young's modulus between MA-BSA/PEG-DA materials with and without solvent exchange.

Figure 3.11. The new mechanical data of MA-BSA materials were plotted back to the Ashby plots with commercial resins. (a) Strain at break-tensile strength plot. (b)Tensile strength-Young's modulus plot.

Figure 3.12. Bar plots showing the swelling ratio of MA-BSA/PEG-DA bioplastics (with no treatment, with TA treatment, and with both TA and heat treatment) after 72-hour swelling in DI water.

List of Tables

Table 1. Printing parameters for MA-BSA/PEG-DA resin on Anycubic Photon Ultra printer.

Table 2. Dynamic light scattering results from MA-BSA syntheses.

Table 3. Mass spectrometry results from MA-BSA syntheses.

Chapter 1. Introduction

1.1. Introduction to Additive Manufacturing

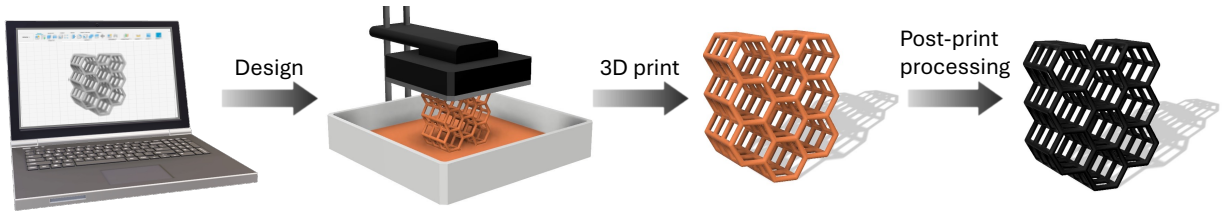

Figure 4.1. Workflow of additive manufacturing. A Computer-Aided Design (CAD) file is first designed and sliced into printable layers. After the part is printed layer by layer, some post-print processing methods are employed to have the desirable mechanical properties.

Additive manufacturing (AM), commonly known as three-dimensional (3D) printing, enables the direct fabrication of physical objects from digital models. Unlike traditional manufacturing methods such as injection molding or subtractive machining, which rely on material removal or formative techniques, 3D printing usually constructs objects in a layer-by-layer fashion and offers numerous advantages over conventional processes.[1,2] Firstly, 3D printing can maximize material-efficiency and significantly reduce material waste. Although supporting structures are sometimes needed, AM can minimize material waste to a great extent. AM is also able to create complex and customized structures, setting it apart from other methods. Since it depends on creating and slicing Computer-Aided Design (CAD) files to build real-world objects, it provides the greatest design freedom, making the most imaginative ideas come true. This ability is particularly valuable for rapid prototyping, where rapid iteration and adjustment are essential in saving time and reducing costs in industry. Combined with all the above advantages, 3D printing has made manufacturing more efficient and accessible for a

variety of applications. Over the past few decades, 3D printing has been widely applied in aerospace[3,4], automotive industries[5–7], healthcare[8–11], art[12], and many other fields. For example, in the dentistry field, it has been largely applied to fabricating metal or ceramic crowns, printing plastic aligners, and designing models for clinical trials and trainings. Upon an easy scanning of patient mouth, lightweight and customized dental objects are simple to produce, and can be produced on demand.[13,14] With the advancement of printer technology and printable materials, the field of 3D printing will continue to advance and become an irreplaceable manufacturing method in the modern world.[15] Therefore I imagine a future where every home will have a 3D printer.

1.2. Vat Photopolymerization

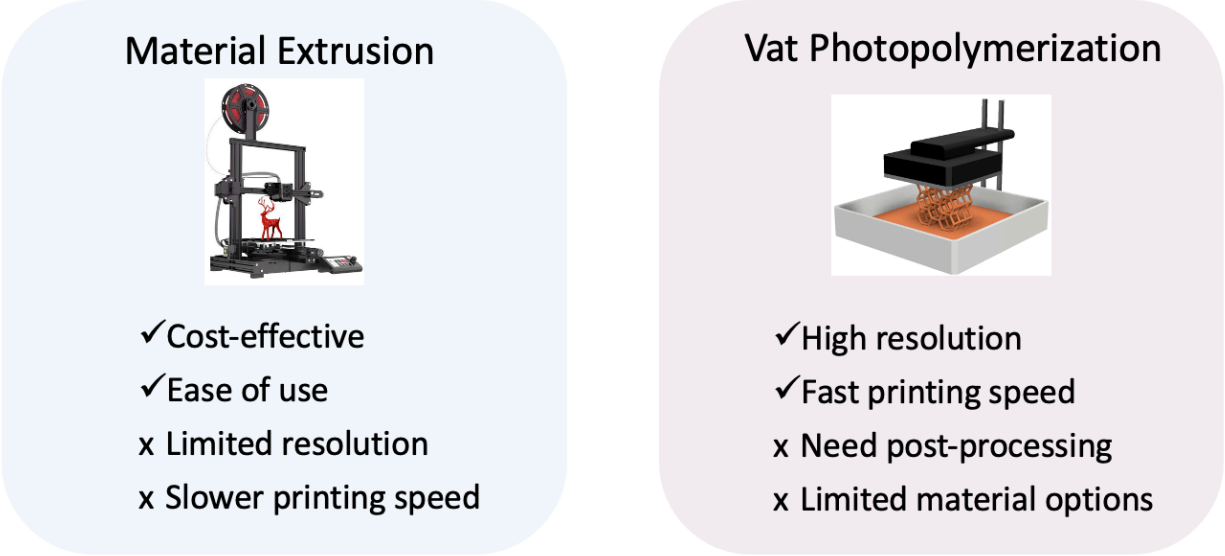

Figure 1.5. Graphical representations of material extrusion (left) and vat photopolymerization (right) and their key features.

Among the most widely used techniques in additive manufacturing are material extrusion and vat photopolymerization (Figure 1.2).[16,17] While material extrusion relies on depositing

filaments layer by layer, vat photopolymerization employs light to selectively cure liquid resin into precise 3D structures. The light, usually at 365 nm or 405 nm, initiates a photochemical reaction in the polymeric resin and quickly solidifies liquid resins to build objects.[18] Common vat photopolymerization techniques include stereolithography (SLA)[19,20], digital light processing (DLP)[21] , liquid crystal display (LCD) printing, two-photon polymerization (TPP), and volumetric printing, to name a few[18,22]. The main difference comes from the light sources that are used in the process, which could be lasers, projectors, or LCD arrays, and those lighting differences lead to differences in printing speed, resolution, and cost. Among various vat photopolymerization techniques, DLP printing stands out for its unique advantages, including high speed, cost-effectiveness, and compatibility with a wide range of printable resins.[23] During DLP 3D printing, the printing head is lowered into a resin-filled vat. A digital projector located underneath the vat is programmed to selectively expose each layer's two-dimensional profile, curing the resin upon light exposure. The solidified layer adheres to the build platform, which then incrementally moves to allow subsequent layers to be formed. This cycle is repeated until the entire object is complete.

Compared to filament-based methods like fused deposition modeling (FDM), vat photopolymerization offers several distinct advantages. First, it provides higher resolution and produces smoother surfaces, which enables the production of highly detailed and complex structures with layer heights down to microscale.[18] This level of precision is particularly valuable for applications requiring fine features, such as microfluidics, dental models, and electronics design. Additionally, vat photopolymerization is significantly faster than extrusion-based methods, especially when using DLP technologies, which simultaneously cure the entire layer area, rather than tracing it line by line. These attributes make vat photopolymerization an ideal choice for industries where precision, speed, and quality are critical.

Despite these advantages, there are also some challenges in vat photopolymerization. The final process of vat photopolymerization often requires post-processing steps, such as

washing uncured resin from the printed object or additional UV curing to achieve the desired mechanical properties. This post-processing washing step usually involves the use of hazardous organic solvents, which require special waste treatment. Additionally, material selection is more limited compared to extrusion-based printing. Material extrusion has demonstrated the ability to print a wide range of materials, including thermoplastics, viscoelastic gels, metals, concrete, and ceramics. In contrast, vat photopolymerization has specific requirements for resins to be printable. Generally, resins must have a relatively low viscosity (around 10 Pa·s) and a fast curing rate when exposed to light. Both low viscosity and fast curing rates have limited the material selection for vat photopolymerization to some extent.[24] Regarding to designing the materials for vat photopolymerization, it has always been a challenge to achieve desirable mechanical properties while controlling photodegradation and minimizing material toxicity.[25] However, there have been increasing advancements in resin formulation, such as modifying polymerization chemistry, adding catalysts, and incorporating photoabsorbers, which are expanding the possibilities for this technology.

1.3. Protein-based Materials

Bioplastic has emerged as a promising solution to address the sustainability challenges caused by plastic pollution. Without a doubt, plastic is considered one of the most influential inventions. Plastics are lightweight, transparent, inexpensive, and applicable across various industries, including use in packaging, electronics, construction and so on. Common synthetic plastics include polyethylene, polypropylene, polystyrene, poly(vinyl chloride) and nylon. However, conventional plastics are mostly derived from petroleum, which is a non-renewable resource that will eventually be depleted.[26] According to statistics, approximately 400 million tons of plastic are produced annually, yet the recycling rate remains as low as 9%, which suggests that the majority of consumed plastics end up as waste.[27] Furthermore, when

petroleum-based plastics are discarded in landfills or the environment, their degradation releases hazardous chemicals and microplastics, which can destroy ecosystems and pose risks to both human health and the environment.[28] A study from Campen and coworkers has shown that environmental microplastics and nanoplastics can accumulate in human brains with a concentration that potentially leads to dementia diagnosis.[29] Those growing concerns highlight the urgent need to transition toward bioplastics as a sustainable alternative.[30]

Bioplastics come from biomass sources such as corn, soy, sugar cane, and protein. As shown in Figure 1.3, the basic idea behind bioplastics is to use natural, renewable resources to create functional materials. After use, these materials can be recycled, upcycled, or biodegraded under specific conditions, significantly reducing waste and environmental impact while promoting a more sustainable ecosystem.[31] Notable examples in 3D printing include resins derived from corn starch and soybean oil. Lactic acid[32,33] from corn starch and epoxidized soybean oil[34,35] can be incorporated as monomers into 3D printing resins, enabling degradation and recycling at the end of their lifecycle, thus supporting the principles of a circular economy. However, their degradation heavily relies on specific environmental conditions and remains relatively inefficient.[36]

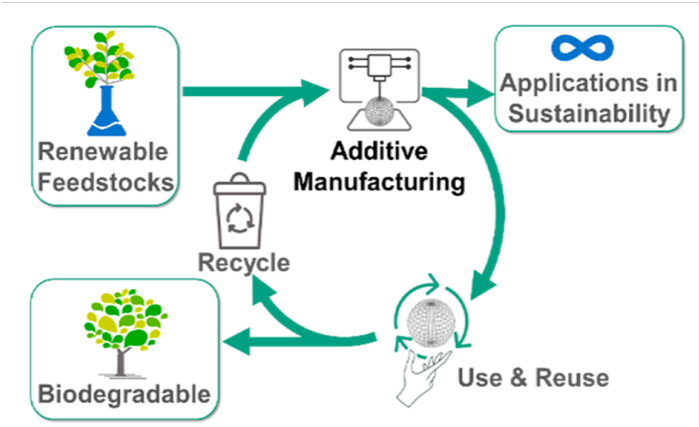

Figure 1.6. Schematic representation of a sustainable additive manufacturing cycle. Renewable feedstocks serve as the primary materials for 3D printing. After use, the printed parts can be reused, recycled, or biodegradable for closed-loop sustainability.[31]

To address these challenges, researchers have turned to bio-based alternatives, such as protein-derived bioplastics. Proteins are natural polymers that are composed of amino acids. By adding proteins to the bioplastic formulations, these materials offer a promising solution due to their renewable nature, biocompatibility, and bifunctionality. One of the main challenges in existing studies lies in the high molecular weight of proteins, which gives difficulties in achieving the desired viscosity for vat photopolymerization. For example, gelatin and silk fibroin have been successfully utilized as materials in DLP 3D printing.[37] Gelatin methacryloyl (GelMA), synthesized from gelatin and methacrylic anhydride, has been extensively studied and is increasingly used in combination with other materials.[38–41] Recently, Qu et al. developed a calcium phosphate (CaP)-based bioink by adsorbing GelMA onto the surface of CaP nanoparticles.[42] The resulting DLP-printed CaP-GelMA scaffolds demonstrated significant potential for bone regeneration and orthopedic repair. Similarly, Park and coworkers were the first example to chemically modified silk fibroin with glycidyl methacrylate to introduce crosslinking sites, enabling its use in DLP printing.[43] The 3D-printed silk fibroin hydrogels were evaluated in both in vivo and in vitro culture systems and showed promising applicability for cartilage tissue engineering.[44]

Despite the proteins that have been discussed above, bovine serum albumin (BSA), a readily available and cost-effective protein, has also gained significant attention. BSA is a single-chain globular protein that consists of 583 amino acid residues. It is derived from biomass and is abundant in nature. The great water solubility and low intrinsic velocity in aqueous solution makes BSA a good candidate for incorporation into 3D printable resin. BSA's secondary structure contains 68% alpha helices and zero beta sheets. The 17 disulfide bonds within the structure help stabilize the tertiary structure of the BSA molecule protein, it is believed that there are 30-35 lysines on the BSA surface that are available for derivatization. By functionalizing or utilizing the surface lysines on the BSA molecule, BSA can be incorporated as

junctions in a polymer network. Upon the addition of crosslinkers and photoinitators, the photo-curable resin based on BSA retains the protein's biocompatibility while achieving properties suitable for 3D printing. This approach not only addresses the environmental and biocompatibility limitations of conventional resins but also opens new possibilities for biomedical applications, such as fabrication of tissue engineering scaffolds and drug delivery systems.

1.4. Objective of Thesis

Conventional petroleum-based 3D printing represents a growing environmental concern, as millions of tons of plastic waste are generated annually and contribute to pollution and ecosystem disruption. This plastic crisis gives rise to the need for sustainable alternatives that reduce environmental harm without sacrificing mechanical performance. One of the major challenges is developing materials that offer the same strength, flexibility, and durability as traditional plastics but with a significantly lower ecological footprint. This is where bio-compatible and biodegradable resins have emerged as key solutions. Bioplastics are designed and engineered for safe use in biological environments, making them ideal for biomedical and healthcare applications as well.

The development of sustainable, high-performance materials like BSA-based bioplastics represents a critical step toward advancing additive manufacturing technologies. By combining the mechanical integrity of traditional materials with the environmental and biocompatibility benefits of bio-based alternatives, these innovations have the potential to drive the next stage of design and production. This work focuses on the understanding and optimization of BSA-based bioplastics, comparing their mechanical properties to those of commercial resins and exploring processing methods to enhance their performance. These aims are separated into two chapters, where the first chapter talks about the comparison of the mechanical properties of

commercial resins and BSA-based bioplastics, and the second chapter focuses on using optimized processing methods to enhance the mechanical properties of BSA-based bioplastics.

Chapter 2. Background and Comparison of Commercial Resins and BSA-Based Materials

2.1. 3D Printing Market Overview

In recent years, the 3D printing industry has expanded rapidly, with an increasing number of companies entering the market and gaining widespread attention across various sectors. Some businesses focus on large-scale, high-efficiency production, aiming to replace traditional manufacturing methods, while others work toward making 3D printing more portable and accessible, positioning it as a household technology. Based on a report from Protolabs in 2024, the 3D printing market is growing at a remarkable rate and is expected to reach a total market value of $57.1 billion within four years.[45] According to the survey, this rapid growth is primarily attributed to the fast production speed and advantages in saving materials and costs of 3D printing. SLA is currently the second most widely used 3D printing technology, following behind FDM, although it only holds a 20% market share now. However, with advancements in technology such as new materials and improved printing techniques, light-based printing is expected to accelerate its development and catch up with traditional FDM. As a result, an increasing number of manufacturing industries are likely to adopt it.

To meet diverse application requirements, scientists and manufacturers have developed a wide range of resin materials, each tailored to specific mechanical and functional properties. Commercial resins for 3D printing can generally be classified into four primary categories based on their mechanical characteristics, as outlined in ISO 527: rigid plastics, semi-rigid plastics, soft plastics, and elastomers.[46] According to ISO 527, materials with a Young's modulus greater than 700 MPa are categorized as rigid plastics, while those with a modulus between 70 MPa and 700 MPa are considered semi-rigid. To the best of my knowledge, there is no official

classification for materials with a modulus below 70 MPa; however, the terms "soft plastic" and "elastomer" are commonly used to describe materials in this range.

Rigid plastics are typically used in high-strength applications where heat resistance, mechanical stability, and minimal deformation are essential. A well-known example is acrylonitrile butadiene styrene (ABS), which is widely used in the automotive and aerospace industries for its durability and thermal stability. These resins offer the structural integrity required for components exposed to mechanical stress and higher temperatures.

Semi-rigid plastics offer a balance between strength and flexibility, making them suitable for engineering components and structural parts that require moderate toughness and some degree of deformation under stress.

Elastomers are highly flexible, rubber-like materials known for their high elasticity and stretchability. They are commonly used in wearable devices and soft robotics. One of the most widely used elastomers in 3D printing is thermoplastic polyurethane (TPU) because of its water resistance, chemical resistance, and high durability. TPU is frequently used in sportswear and footwear. A notable example is Rebound Resin, developed by New Balance for high-performance shoe components, illustrating the expanding role of advanced resins in athletic and performance gear.

The wide variety of 3D printing materials reflects the adaptability of this technology, which can be used to produce functional parts in industries such as aerospace, automotive, healthcare, sportswear, and consumer electronics. As the field continues to advance, the development of specialized resin formulations will further broaden its application range, providing numerous solutions for a variety of engineering and commercial needs.

2.2. Ashby Plots for Material Selection

Ashby plots, first developed by Prof. Mike Ashby in 1992, are useful and informative tools for screening materials' properties early in their life cycle.[47] They are a type of scatter plot in which the data points are grouped by bubbles, enabling more efficient screening compared to numerical data analysis. A classic application is the Young's modulus versus density plot (Figure 2.1), which clearly distinguishes performance boundaries across material classes, particularly useful for lightweight design optimization.[48,49] By graphically presenting key property relationships, Ashby plots provide the rapid identification of suitable material candidates while revealing critical trade-offs between competing mechanical characteristics.

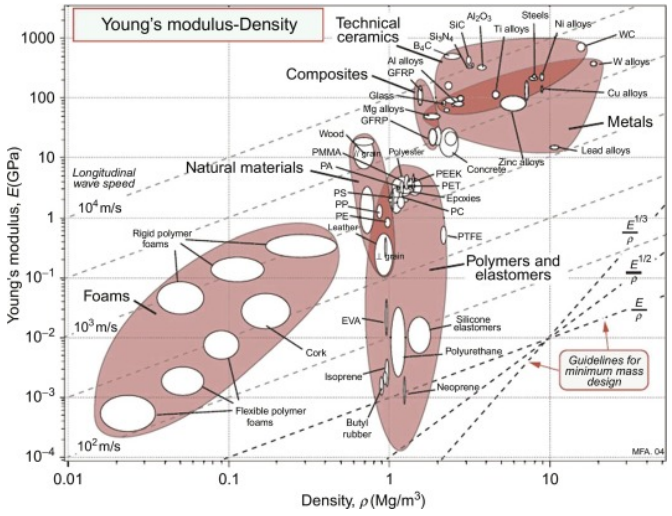

Figure 2.2. An example of an Ashby plot that illustrates the relationship between Young's modulus and density across a range of material classes, including metals, polymers, foams, natural materials, and composites.[47]

2.2.1. Stress-strain Curve

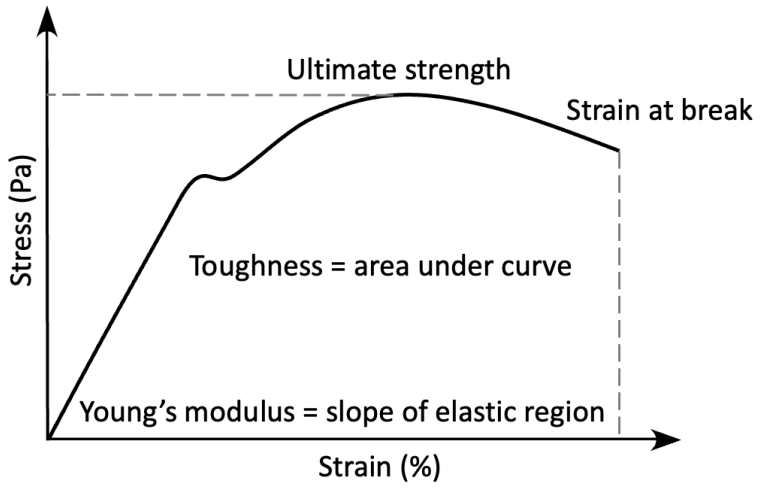

Figure 2.2. Stress–strain curve illustrating the mechanical behavior of a plastic material. Slope of the linear elastic region defines Young's modulus. After reaching the yield point, irreversible plastic deformation begins and necking until the material ultimately breaks apart. Toughness is calculated to be the area under stress-strain curve.

The tensile stress-strain plot, often used to analyze elongation and ultimate tensile strength, is a key tool for studying the mechanical properties of plastics. When increasing tensile force is applied at a constant stretching speed, the material stretches and deforms, allowing stress and strain to be measured over time as shown in Figure 2.2. A typical stress-strain curve for plastics begins with a linear region at low strain levels. Here, the material deforms elastically, meaning the deformation is recoverable. The slope of this linear portion is Young's modulus, which indicates stiffness—higher values suggest a stiffer material. Beyond this elastic region, the material reaches its yield stress, and irreversible deformation such as necking begins until breakage. Brittle plastics tend to fracture at low strain. On the other hand, softer materials often break at higher strain but lower stress. This makes the elongation and ultimate tensile strength

plot a valuable tool for evaluating the tensile performance of plastics made from commercial resins.

2.3. Trends and Observations

A total of 140 commercial resin products from 8 printing companies (Anycubic, Formlabs, Elegoo, Siraya, Esun, Sunlu, and Carbon) were analyzed. Among these commercial resins, 3% are plant-based, typically derived from corn and soybean oil, while 27% are biocompatible resins, commonly used for dental and medical applications. The most frequently reported properties include ultimate tensile strength, Young's modulus, flexural strength, flexural modulus, heat deflection temperature, Shore hardness, elongation at break, density, and notched impact strength. In this case, tensile strength, elongation at break, and Young's modulus are used to be directly compared across materials since those are the available data on BSA-based material as well. In Figure 2.3 (b), rigid materials are concentrated in the region of high strength and low elongation, whereas elastomers exhibit high elongation but low tensile strength. Semi-rigid resins occupy the intermediate region between these two extremes. Figure 2.3 (c) displays tensile strength versus Young's modulus. Rigid resins are primarily located in the high-modulus range, while semi-rigid and elastomeric resins exhibit significantly lower stiffness. These plots highlight the trade-offs between stiffness, strength, and flexibility among different resin categories.

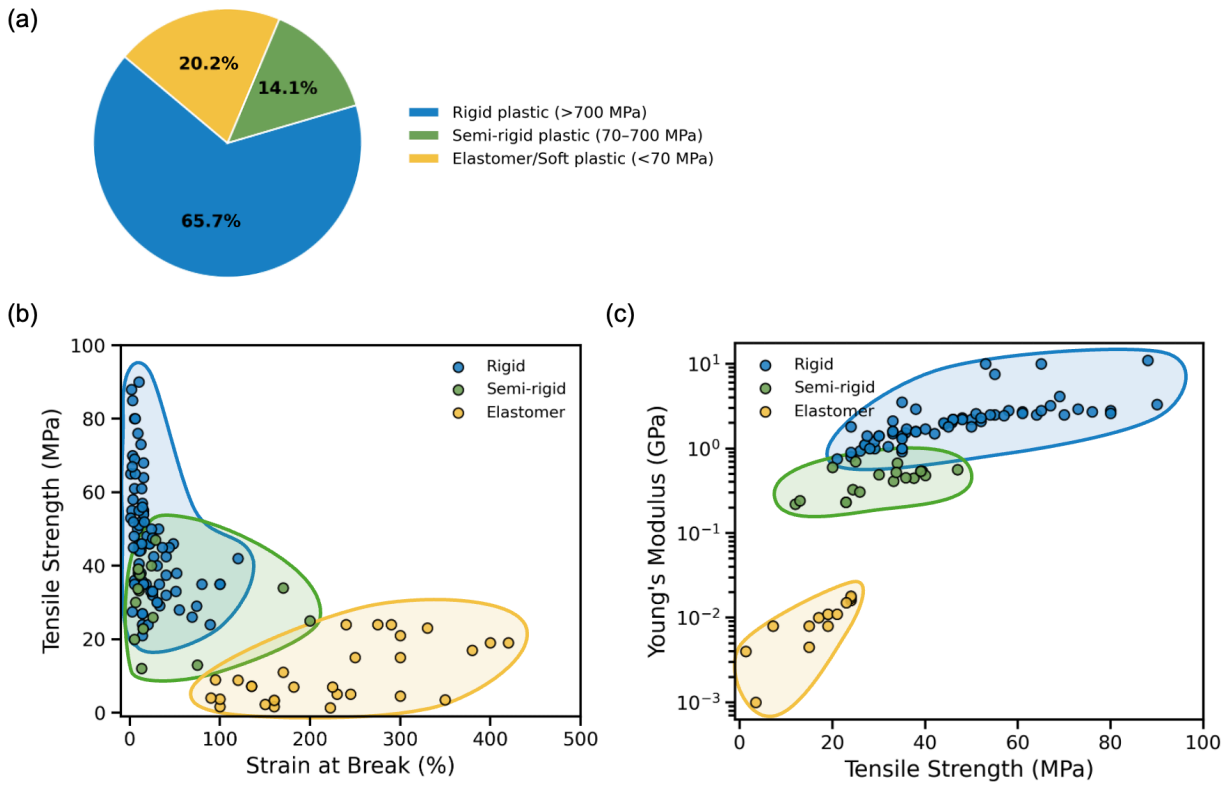

Figure 2.3. (a) Pie chart for the distribution of material types—rigid plastics (65.7%), semi-rigid plastics (14.1%), and elastomers (20.2%) — within the compiled mechanical property dataset from this study. (b) An Ashby plot comparing tensile strength and strain of commercial resins. (c) An Ashby plot comparing tensile strength and Young's modulus of commercial resins.

2.4. Background on BSA-based Materials in Nelson Lab

2.4.1. Methacrylated BSA (MA-BSA)[50,51]

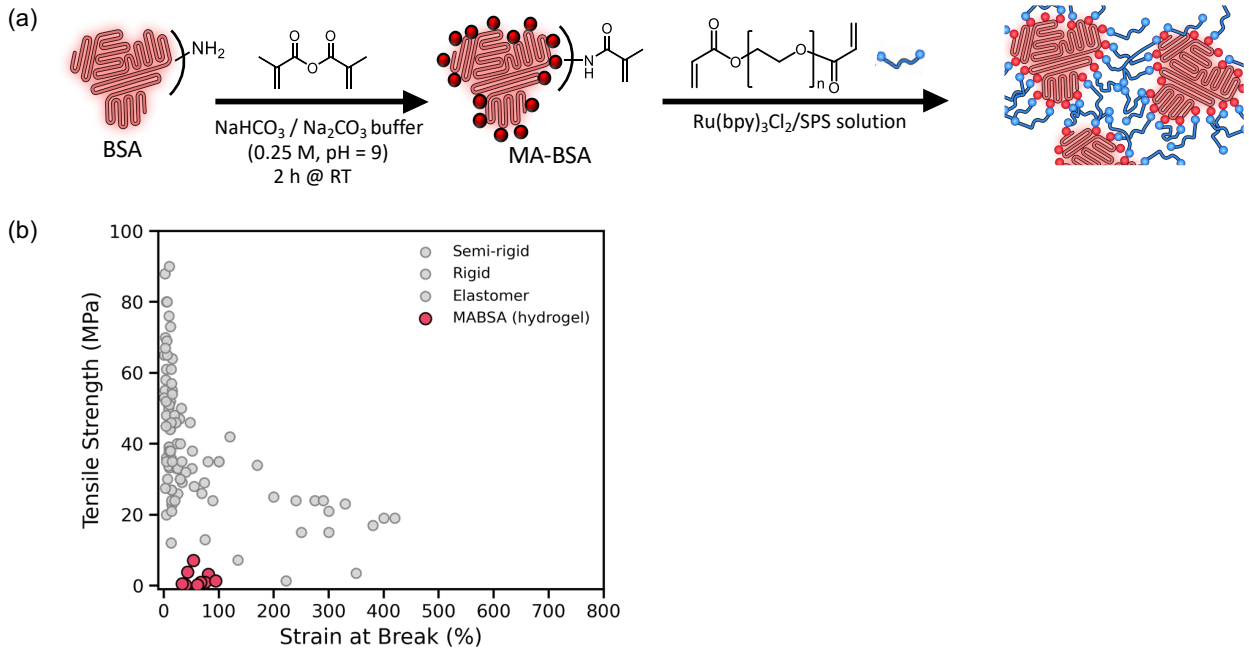

Figure 2.4. (a) Schematic showing the steps of preparing MA-BSA/PEG-DA resin from methacrylation and radical polymerization. (b) Ashby plot comparing tensile strength and strain at break for MA-BSA-based hydrogels against commercial resin categories.

The first BSA-based bioplastic was fabricated using methacrylated MA-BSA. Methacrylate chemistry has been widely used for radical polymerization due to its fast reaction rate in photocuring. In this process, the lysine groups on the BSA surface were functionalized with methacrylic anhydride through methacrylation to produce MABSA. The degree of functionalization was calculated using the 2,4,6-trinitrobenzene sulfonate (TNBS) assay and found to be approximately 85–95%. Three different comonomers (acrylamide, hydroxyethyl acrylate, and PEGDA) were also investigated as a comparison. Under 405 nm light, the ruthenium and persulfate complex initiated the polymerization and crosslinked the acrylate/methacrylate chain ends.

2.4.2. BSA/PEG-DA Bioplastics[52]

To simplify the fabrication process and eliminate the need to synthesize MABSA, which reduces the overall time by skipping macromonomer synthesis, a polymer network was created directly from BSA and PEG-DA via aza-Michael addition. The photoinitiator Lithium Phenyl (2,4,6-trimethylbenzoyl) phosphinate (LAP) was added to help with the free radical polymerization. The BSA-based bioplastics consists of 75 wt% MABSA and 25 wt% PEG-DA in a 3:1 ratio was shown to have a great mechanical property while retaining material processability.

2.4.3. BSA/PEG-DA Bioplastics with Additives[53]

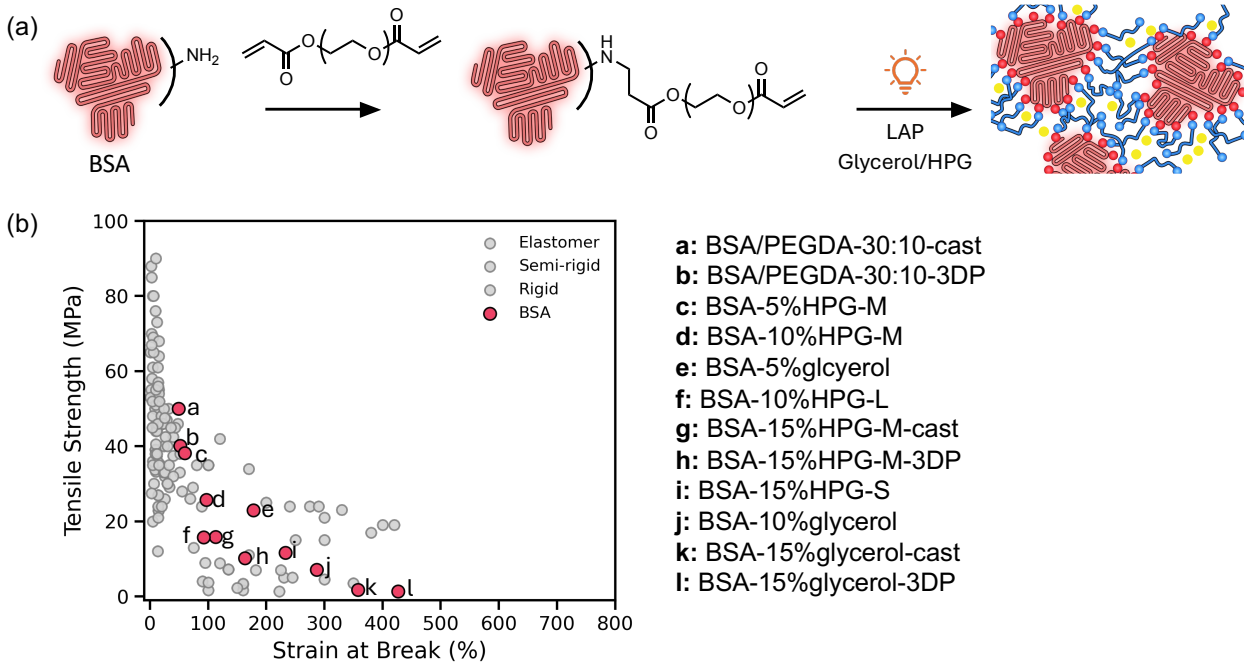

Figure 2.5. (a) Schematic showing the BSA/PEG-DA resin from Michael addition and network formation. (b) Ashby plot comparing tensile strength and strain at break for BSA/PEG-DA bioplastics with various concentrations of glycerol or hyperbranched poly(glycerol)s as additives against commercial resin categories.

Building on the BSA-PEGDA network system, the effects of adding plasticizers were also investigated. Glycerol was chosen as the additive due to its water solubility and compatibility with the BSA-PEGDA matrix. Experiments were conducted using varying concentrations and molecular weights of glycerol and hyperbranched poly(glycerol)s (HPGs) to study their impact on the material properties. It was showed that there was a linear increase in strain at break with increasing concentration of the additives that were used. The glycerol and HPGs demonstrated their ability to provide flexibility to the polymer network as plasticizers.

2.4.4. Norbornene-BSA (NB-BSA) Bioplastics

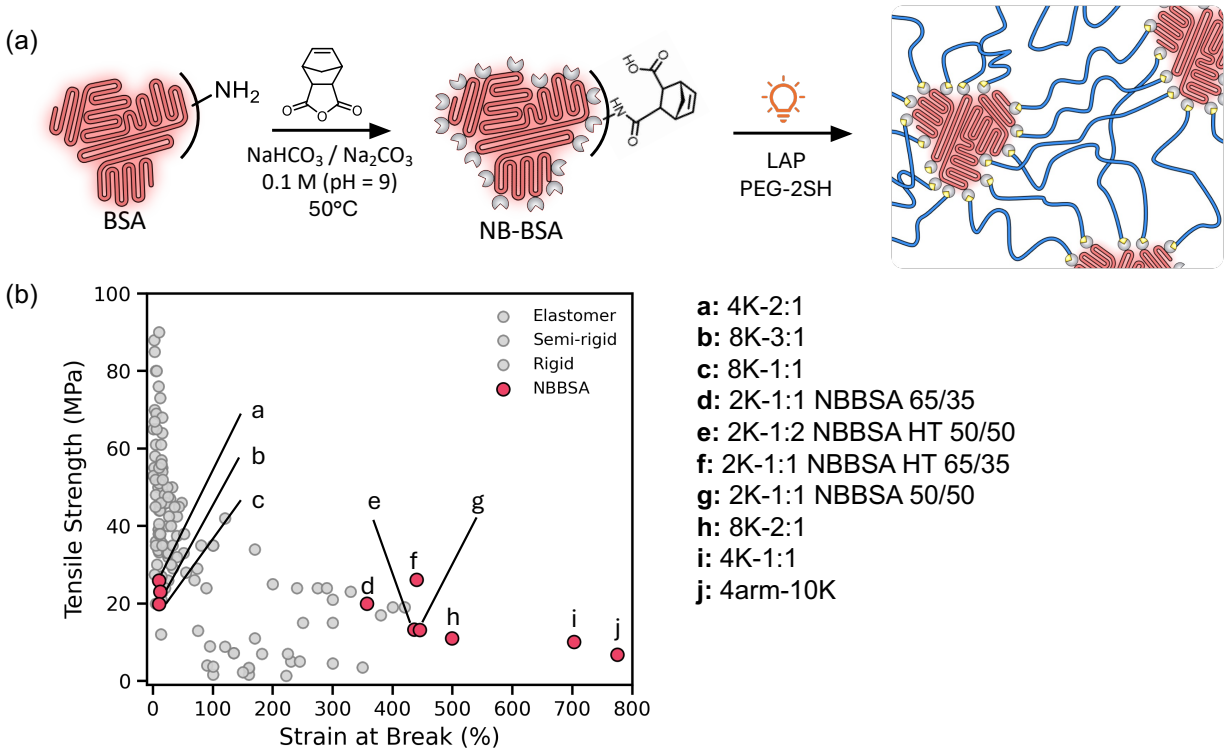

Figure 2.6. (a) Schematic showing the NB-BSA/PEG-2SH thiolene chemistry to form polymer network. (b) Ashby plot comparing tensile strength and strain at break for NB-BSA/PEG-2SH bioplastics against commercial resin categories.

Instead of relying on amidation reactions to functionalize lysine groups and acrylate chemistry for crosslinking, an alternative approach using thiol-ene click chemistry was explored. The previous acrylate-based chain growth polymerization usually leads to heterogeneous network that contains loops and dangling ends, and thus lower the mechanical intergrity.[54] In this method, lysine residues on the surface of BSA were functionalized with carbic anhydride to introduce norbornene groups. PEG was modified to have thiol end groups and employed as a crosslinker.[55] The norbornene groups on BSA then reacted with the PEG-2SH crosslinkers to form a polymer network through step-growth polymerization. This thiol-ene network offers a more defined and controlled structure compared to the methacrylated system, as the latter can lead to uncontrolled loops and longer crosslinker chains due to the propagation of PEGDA with itself. Although loops can still form in the thiol-ene system (e.g., when a PEG-2SH reacts with two norbornene groups on the BSA surface), the overall network is more precise and predictable. Other than modifying the polymerization chemistry, the effect of using various molecular weight of PEG-2SH, ratios between protein and polymer, and additional heat treatment were studied. In this NB-BSA/PEG-2SH system, an exceptional strain at break was observed. As their capabilities to have a strain at break in the range of 400% to 800%, they outcompete the all the commercial resins that I analyzed.

2.4.5. NB-BSA Double Network Bioplastics

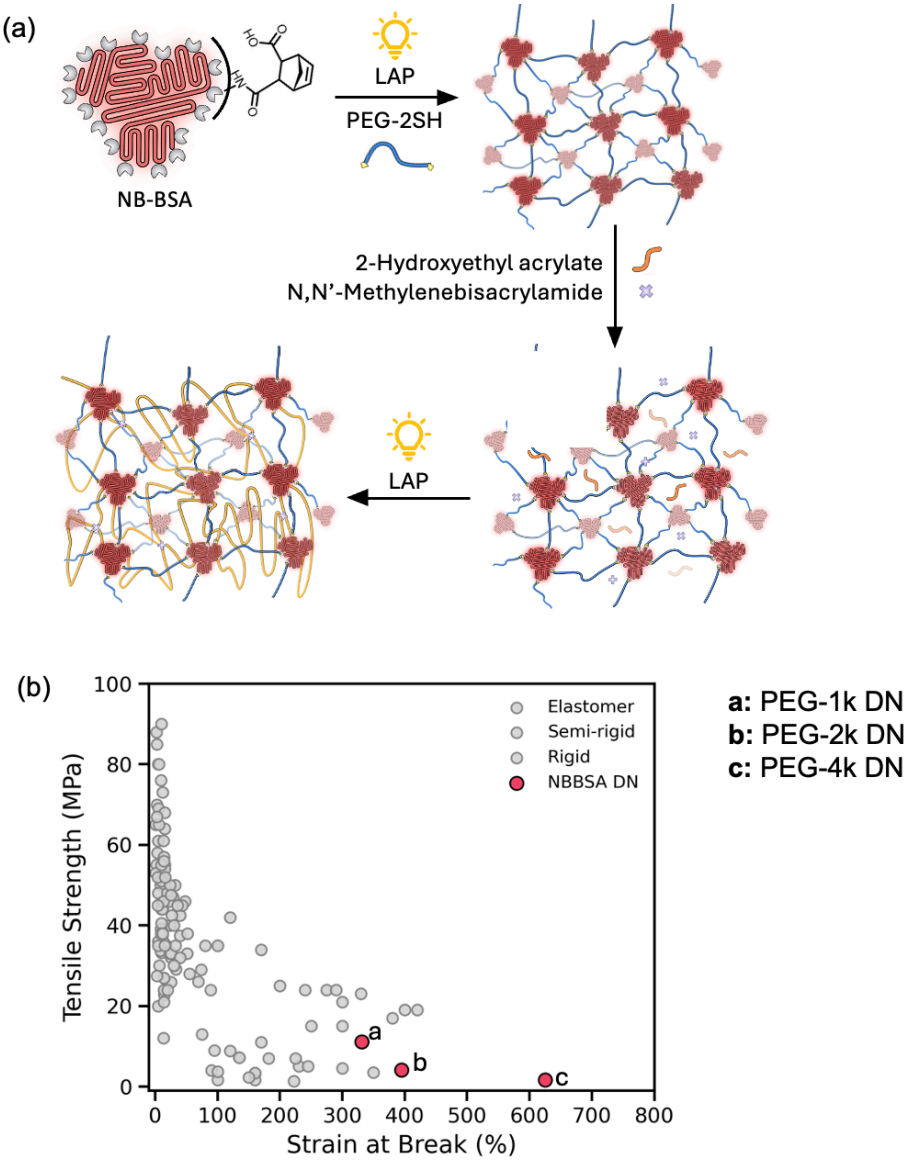

Figure 2.7. (a) Schematic showing the formation of NB-BSA double network. (b) Ashby plot comparing tensile strength and strain at break for NB-BSA double network bioplastics against commercial resin categories.

A double network (DN) bioplastic formulation was also developed using the NB-BSA and PEG-2SH system as the foundation. In this system, the NB-BSA and PEG-2SH polymer matrix serves as the first network, which is rigid and brittle. A second network, composed of 2-

hydroxyethyl acrylate (2-HEA) monomers and the crosslinker N,N'-Methylenebisacrylamide, is incorporated and loosely crosslinked to enhance the material's mechanical properties. This double network system showed advantages in better dissipating energy while resisting from fracture. The effects of crosslinker length were explored to show that longer PEG-2SH chain in the first network led to lower strength but higher strain at break.

2.5. Comparative Analysis Between BSA-based Materials and Commercial Resins

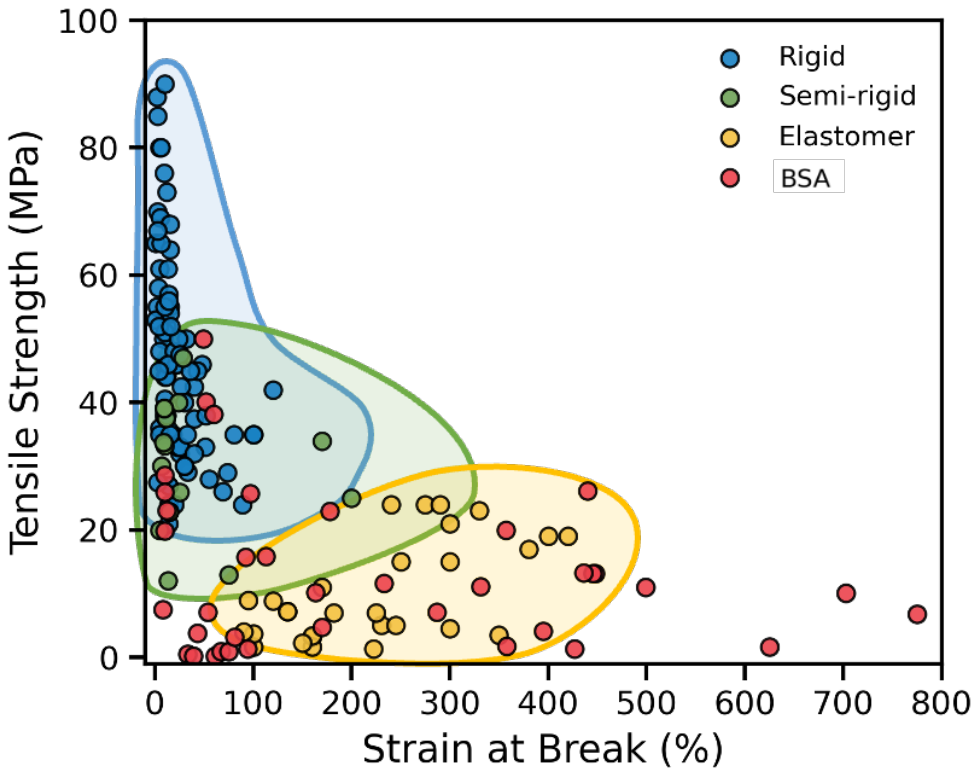

Figure 2.8. Ashby plot comparing tensile strength and strain at break for BSA-based bioplastics against commercial resin categories.

The advantages of BSA-based materials are significant. They exhibit tunable mechanical properties, spanning a broad range on the Ashby plot. Several BSA-based materials demonstrate a unique combination of higher tensile strength and greater elongation

simultaneously, surpassing the performance of many commercial resins. On the Ashby plot, data points that are shifted upward and to the right represent materials that are both stronger (higher tensile strength) and more ductile (greater elongation), which is a particularly promising finding.

However, BSA-based materials also have some limitations. First, their strength performance is constrained. While many BSA data points fall within the elastomer region on the Ashby plot, they do not behave like true elastomers. Instead, their properties align more closely with those of soft plastics rather than rubber-like materials. Secondly, BSA-based bioplastics exhibit inconsistent performance. Notably, they are highly susceptible to moisture absorption from the atmosphere, which restricts their use in environments where exposure to water could compromise their mechanical properties. They also tend to swell when exposed to aqueous solutions. Additionally, during the drying process of 3D-printed hydrogels into bioplastics, issues such as warping and bending of the structures can arise. The dimension of printed object would shrink around 60% as well. Dehydration is a critical step that largely influences the final performance of these materials.

Chapter 3. Optimized Processing Methods for MA-BSA-based Bioplastics

To overcome the limitations of BSA-based bioplastics, such as reswelling in aqueous solutions and rehydration that significantly reduces mechanical performances and limits their medical applications, additional processing methods are needed. Previous studies conducted by Smith et al. have shown that the mechanical properties of MABSA-based tough hydrogels can be improved by post-printing methods, such as TA treatment and heat treatment.[51] Tannic acid, a plant-sourced polyphenol, has been extensively used as an additive in materials for its nature properties, such as wound healing, high-water solubility, and adhesiveness.[56] It has been shown that TA can provide secondary crosslinks within material by hydrogen bonding and supramolecular conjugation to proteins like gelatin and albumin.[56,57] Furthermore, heat treatment that promotes protein denaturation and beta-sheet formation can add additional non-covalent bonding to enhance the ultimate strength, elastic modulus, and toughness of BSA-based materials. Smith et al. have successfully demonstrated these optimized processing methods can be used to fabricate tough 3D-printed hydrogels, but the mechanical profiles of those MA-BSA bioplastics need further investigation.

3.1. Materials and Experimental Methods

3.1.1. Materials

Reagent grade and fatty acid-free BSA powder was purchased from Proliant. Methacrylic anhydride (94%), tris(2,2′-bipyridyl)-dichlororuthenium(II) hexahydrate [$Ru(bpy)_3Cl_2$] (99.95%), poly(ethylene glycol) diacrylate (Mn 700 Da), 2-hydroxyethyl acrylate (99%), and sodium persulfate (SPS) (98%) were purchased from Sigma Aldrich and used as received.

3.1.2. MA-BSA Synthesis

In a 1 L round bottom flask, BSA (20g) was added to 200 mL of sodium carbonate-bicarbonate buffer (0.25M, pH9), and the mixture was stirred until the BSA solid was fully dissolved. Then methacrylate anhydride (4mL) was added to the flask dropwise using a syringe. After the reaction was run at room temperature for 2 hours while stirring, it was diluted 2-fold with DI water. Then the product was dialyzed against DI water for 48 hours using dialysis tubing with MWCO of 12-14 kD. Following dialysis, the solution was freeze-dried using liquid nitrogen. After lyophilizing the MABSA product for 3 days, it was collected and stored at 4 °C until use.

3.1.3. Dynamic Light Scattering (DLS)

The DLS sample was prepared in 1× phosphate-buffered saline (PBS) solution at a concentration of 10 mg/mL. Then, it was filtered through a 0.22 μm cellulose acetate syringe filter. The DLS experiment was performed at 25 °C with 1.2 mL of sample solution in a quartz cuvette.

3.1.4. Liquid Chromatography Tandem Mass Spectrometry (LC-MS/MS)

The mass spectrometry sample, BSA or MA-BSA, was prepared by dissolving it in DI water at a concentration of 1 mg/mL. The sample was analyzed using an LC gradient on an Agilent PLRS protein column with 20 μL injections using the AB SCIEX TripleTOF 5600 system.

3.1.5. Resin Preparation Protocol

The resin consists of 30 w/w % MA-BSA, 10 w/w % PEG-DA(700) or 2 w/w % 2-HEA as comonomers, 0.075 w/w % Tris(2,2'-bipyridyl)ruthenium(II) chloride hexahydrate, 0.24 w/w % Sodium persulfate as deionized (DI) water as solvent. In short, to prepare a 5 g MABSA-PEGDA resin, 0.5 of PEG-DA(700) was first dissolved in a 50 mL centrifuge tube containing 2.8 g of DI water, and 1.5 g of MA-BSA was slowly added to the tube in three portions. The mixture was shortly vortexed and put on a shaker to get fully dissolved, and the tube was covered with foil and stored at 4 °C overnight. The photoinitaors were prepared separately in stock solutions as a concentration of 37.4 mg/ml for $Ru(bpy)_3Cl2$ and 119 mg/ml for SPS. 100 uL of each photoiniator stock solutions were added to the centrifuge tube upon printing or casting.

3.1.6. 3D Printing Parameters

Table 4. Printing parameters for MA-BSA/PEG-DA resin on Anycubic Photon Ultra printer.

Layer thickness (mm)	0.1	Anti-alias	4
Exposure time (s)	10	Z lift distance (mm)	5
Off time (s)	1	Z lift speed (mm/s)	2
Bottom layers	4	Z retract speed (mm/s)	2

3.1.7. Mechanical Testing of MA-BSA/PEG-DA Bioplastics

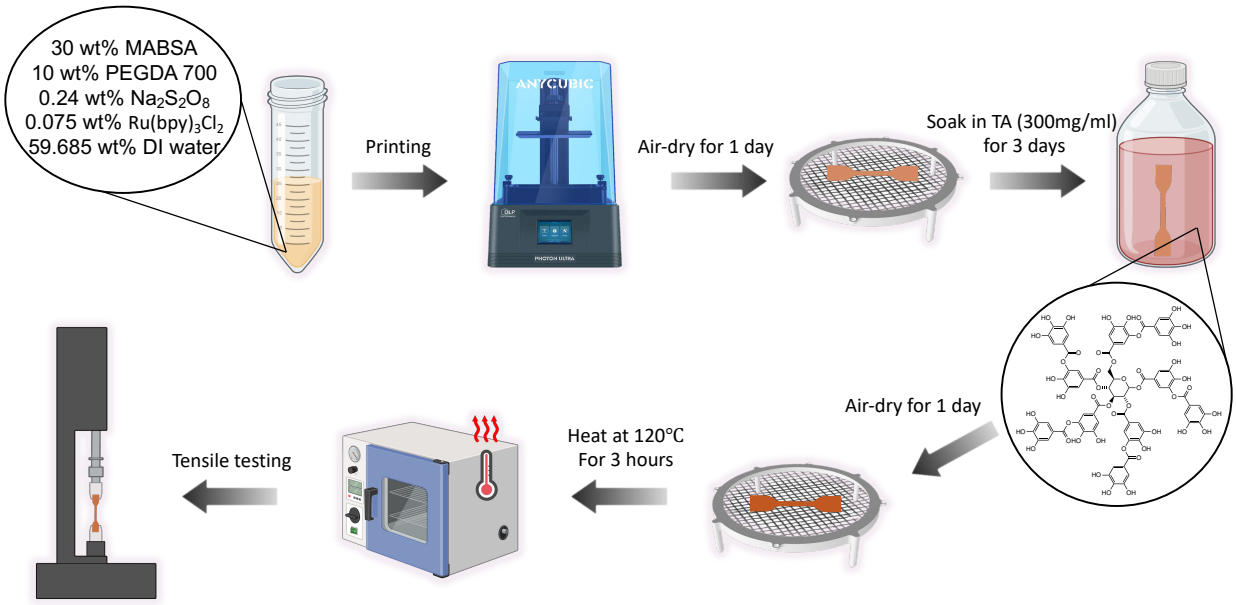

Figure 3.1. A schematic workflow of MA-BSA/PEG-DA bioplastics sample preparation.

The dumbbell-shaped MA-BSA sample was dehydrated for 24 hours by air drying, and then was soaked in a 300 mg/mL tannic acid (TA) solution for 3 days to let TA infuse into and bond the network. After a gentle rinse to remove the excess TA solution using DI water, the sample was air-dried for 24 hours again. Then the sample was heated at 120 °C for 3 hours in an oven to introduce protein denaturation. The tensile properties of the materials were tested at room temperature with a tensile speed at 5 mm/min using an Instron 5585H load frame with a 1 kN load cell and flat pneumatic grips. The tests were repeated at least three times for each group of samples.

3.1.8. Attenuated Total Reflection Fourier Transform Infrared (ATR-FTIR) Spectroscopy

Fourier transform infrared (FTIR) spectroscopy with attenuated total reflection (ATR) mode was conducted using a PerkinElmer Frontier spectrometer fitted. Each spectrum was obtained by averaging 128 scans at a spectral resolution of 16 cm^{-1} within the range of 2000 to 1000 cm^{-1}. Data acquisition and processing were performed using PerkinElmer Spectrum software. All spectra were normalized based on their respective maximum absorbance peaks.

3.1.9. Swelling Ratio of MA-BSA/PEG-DA Bioplastics

Cylinders (10mm x 5mm) were printed using MA-BSA/PEG-DA resin on an Anycubic Photon Ultra DLP printer. The samples were air-dried 24 hours and allowed to dehydrate to bioplastics, and some samples were further treated with TA and heat. The diameters and heights of bioplastics were measured using a digital caliper to calculate the initial volume, $V_{initial}$. To achieve equilibrium swelling, the cylinder samples were submerged in DI water for 72 hours and then the final volumes, $V_{final,}$ were calculated. The swelling ratio was calculated based on Equation 1 below.

$$\text{swelling ratio} = \frac{V_{final} - V_{initial}}{V_{initial}} \times 100\% \quad (1)$$

3.2. Results and Discussion

3.2.1 MA-BSA Characterization by Dynamic Light Scattering

Prior to methacrylation, dynamic light scattering (DLS) was performed on the BSA reagent to track the changes resulting from the addition of methacrylate groups to the BSA

surface. The DLS analysis of pure BSA revealed an average hydrodynamic diameter of approximately 8.469±0.4094 nm, with a polydispersity index (PDI) of about 0.088. In contrast, the synthesized MABSA exhibited an average hydrodynamic diameter of around 9.029± 0.535 nm, with a PDI of about 0.115±0.009685. The slight increase in hydrodynamic diameter provides evidence of successful functionalization, as the methacrylate group is larger in size compared to the lysine residue it replaces. Moreover, the low polydispersity index indicates that the synthesized MA-BSA retains its compact globular structure, similar to that of unmodified BSA. Both the size and PDI are critical parameters for characterizing MA-BSA. If denaturation or aggregation had occurred during the synthesis process, the DLS plot would have displayed two peaks at larger hydrodynamic diameters, accompanied by a significantly higher polydispersity index.

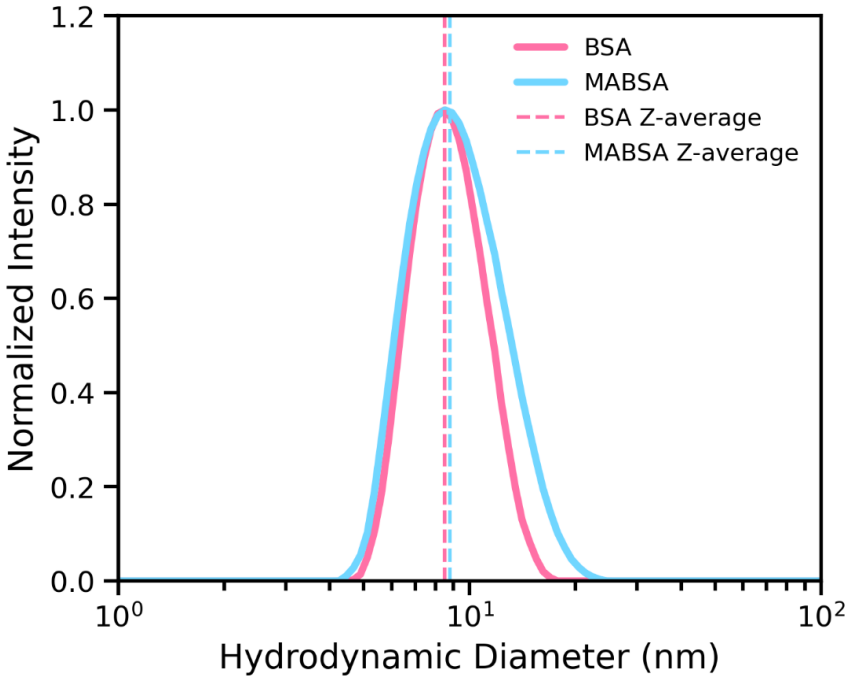

Figure 3.2. Dynamic light scattering spectrum showing the particle size distribution of pure BSA and synthesized MA-BSA.

Table 5. Dynamic light scattering results from MA-BSA syntheses.

MA-BSA synthesis	Dynamic Light Scattering (DLS)	
	Z-average (d. nm)	PDI
MZ-1-5	8.179	0.100
MZ-1-8	10.39	0.271
MZ-1-15	9.130	0.126
MZ-1-20	9.341	0.113
MZ-1-24	9.580	0.120
MZ-1-26	8.915	0.114

3.2.2. MA-BSA Functionalization by Mass Spectrometry

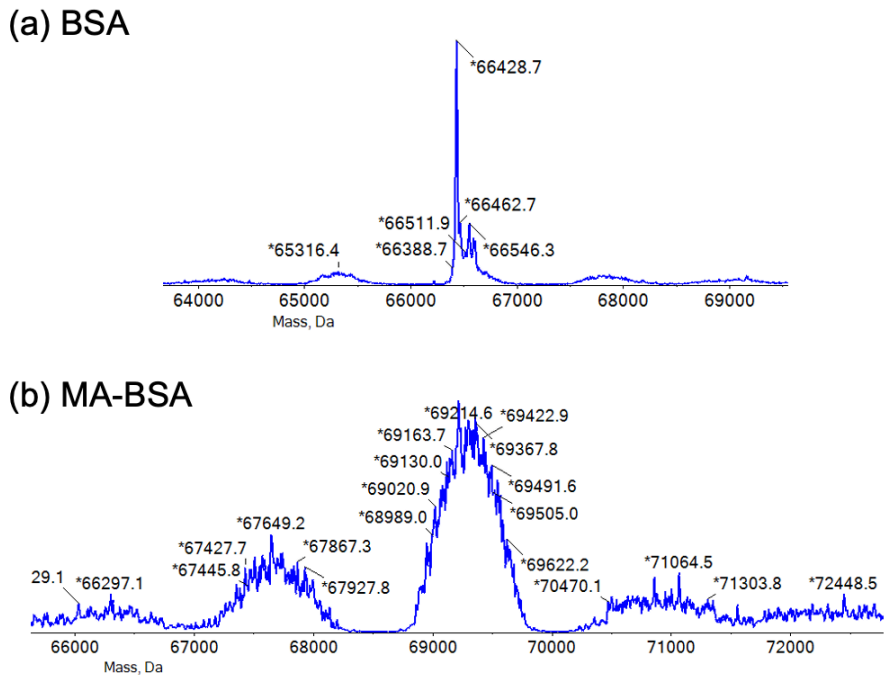

Figure 3.3. Mass spectrum of (a) BSA and (b) synthesized MA-BSA.

BSA is known to have a molecular weight of 65 kDa, with 30–35 lysine residues available for reaction. Given this, we believe mass spectrometry will be a valuable tool for visualizing the functionalization of BSA through amidation by observing the mass difference. As shown in Equation 2, the degree of functionalization can be estimated by calculating the mass difference between MA-BSA and BSA and dividing this value by the mass of a methacrylate group. This approximates the number of methacrylate groups attached to the BSA molecule.

For the mass spectrometry analysis, the mass spectrum of unmodified BSA displayed one major peak at approximately 66,429 Da, accompanied by two minor peaks nearby. Following the amidation reaction, where methacrylate groups were introduced to the BSA surface, all three peaks shifted to higher molecular weights. This shift indicated an average functionalization of approximately 29–34 methacrylate groups per BSA molecule. However, the peak intensities increased unevenly, with the left minor peak becoming significantly larger than expected. The calculated functionality represents an average value, primarily based on the masses of the left and central peaks.

$$\text{Functionalization} = \frac{\text{MW}_{\text{MA-BSA}} - \text{MW}_{\text{BSA}}}{\text{MW}_{\text{MA}}} \quad (2)$$

Table 6. Mass spectrometry results from MA-BSA syntheses.

MA-BSA synthesis	**Mass Spectrometry (MS)**
	Functionalization (MA per BSA)
MZ-1-5	~29
MZ-1-8	~30

MZ-1-15	~32
MZ-1-20	~30
MZ-1-24	~34
MZ-1-26	~31

3.2.3. 3D Printing

The MA-BSA/PEG-DA bioplastics were 3D-printed using an Anycubic Photon Ultra DLP printer. To initiate the printing process, I utilized the parameters previously optimized for BSA/PEG-DA resin on the same printer: a layer thickness of 0.100 mm, 8 seconds of normal and bottom exposure time, and 1 second of off time. All other parameters were maintained as default settings in the Anycubic slicing software. A complex structure, featuring rectangles of varying thicknesses, holes of different sizes, and a slope known to be challenging to print due to its dependence on resin viscosity and printing parameters, was fabricated to evaluate the printer's capability. The printed hydrogel was subsequently examined under a microscope as shown in Figure 3.4.

From the observations, an exposure time of 8 seconds demonstrated good printability for the rectangular sections but exhibited slight undercuring in the slope region. To address this, I increased the exposure time to 9 seconds and then to 10 seconds. However, no significant improvements were observed in terms of smoother slopes or clearer holes. This issue might be attributed to the resin being reused beyond its optimal lifespan, as the photoinitiator used in the resin is sensitive to both temperature and light. During the printing process, as the UV light continuously cured the resin, the photoinitiator became increasingly reactive, propagating

through the polymer networks. This caused the resin's viscosity to increase over time as the polymer crosslinked, even within the resin tray. Consequently, at 10 seconds of exposure, some over-curing was observed in the hole regions. After 30 minutes of air drying, the structures printed with 8-second and 9-second exposure times exhibited cracking, while the structures printed with 10 seconds of exposure remained intact.

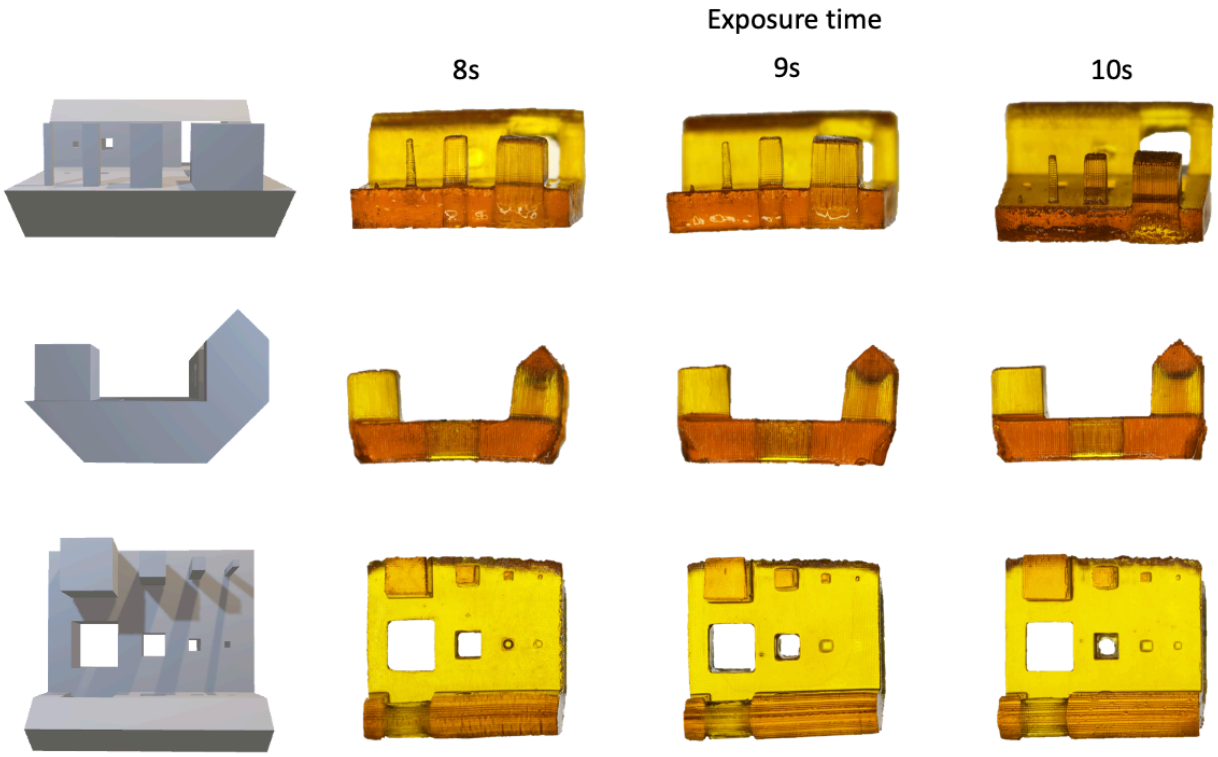

Figure 3.4. Microscopic images of printed structures with various holes and voids evaluated at three exposure times (8s, 9s, and 10s). Three viewing angles were monitored to assess dimensional fidelity and resolution. CAD models are shown in the leftmost column for comparison with the actual printed results.

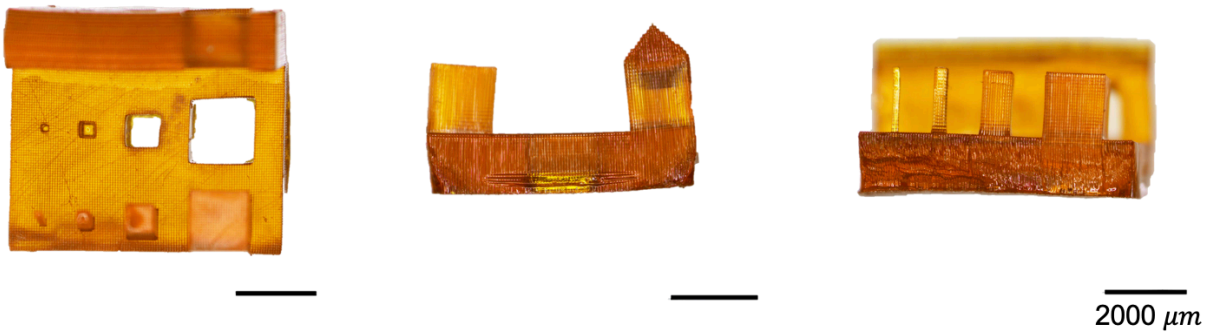

Figure 3.5. Microscopic images of MA-BSA/PEG-DA bioplastic structures printed with an exposure time of 10 seconds. The printed samples were imaged after 24 hours of air drying.

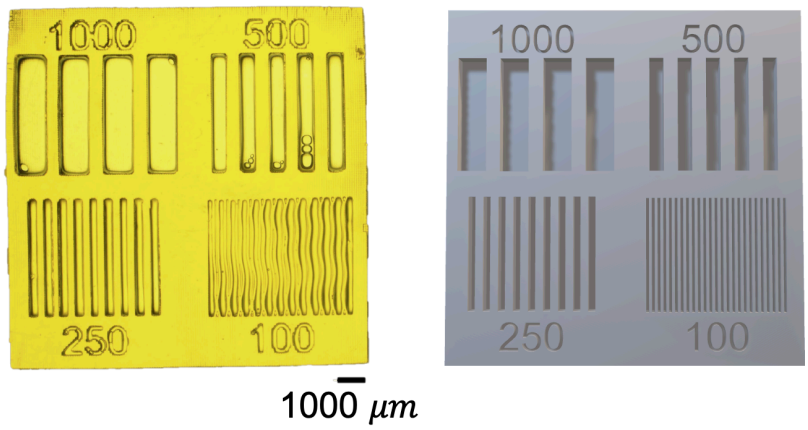

Figure 3.6. Resolution test for MA-BSA/PEG-DA materials printed with line widths of 1000, 500, 250, and 100 μm. The left image shows the microscopic view of the printed sample, while the right image displays the corresponding CAD design.

To address the issues caused by reusing the resin, I retested the printing process using a 10-second exposure time with fresh resin. As shown in Figure 3.5, the scratches observed on the printed structures were attributed to imperfections on the printing head, which had pre-existing scratches and was not perfectly flat. All four pillars were successfully printed,

demonstrating the printability of the resin under these conditions. In addition to the overhanging structure, a rectangle featuring defined lines and voids was also printed to evaluate the resolution capabilities (Figure 3.6). The printing process successfully achieved a resolution down to 250 μm, and nearly 100 μm in some areas. The current results demonstrated that the resin can already print complex and fine structures using this commercial printer. Future improvements in print fidelity could be achieved by adding a photoabsorber or optimizing other printing parameters such as lift and retract speed.

3.2.4. Tensile Testing

To reproduce data previously reported for tough hydrogels, I first tested different fabrication procedures to identify optimal conditions for producing bioplastics via dehydration of hydrogels. To minimize material usage during preliminary testing, resins containing 30 wt% MA-BSA and 2 wt% HEA were cast into polydimethylsiloxane molds to create dogbone-shaped specimens for mechanical testing. These samples were soaked in DI water for 24 hours to form hydrogels before tensile testing. At least three replicates were tested per condition, though some samples were discarded due to defects. Foam was placed between the grips and dogbone specimens to increase friction and prevent slipping during tests. In the Figure 3.7, the pink curve represented the tensile data obtained using the original procedure. The samples exhibited a Young's modulus of 67.11±6.50 MPa and an ultimate tensile strength of 4.11±0.51 MPa. Compared to literature values, the modulus was 43% lower, and the tensile strength was reduced by 42%, indicating a significant deviation in mechanical performance.[51]

Therefore, to improve mechanical performance, I explored several modifications: an additional swelling step post-TA treatment, clamping dogbone samples with glass slides, and increasing specimen thickness. The additional 24-hour DI water soak aimed to remove residual monomers, photoinitiators, and unbound TA compounds, which resulted in slight increases in

both tensile strength and elongation (green curve). Using two glass slides to sandwich the dogbones reduced bending during drying; however, surface warping persisted due to uneven hydration and dehydration steps during the fabrication process, yielding a tensile strength of 3.99±0.32 MPa and elongation of 0.24±0.01 mm/mm (blue curve). I hypothesized that differences in specimen thickness may have contributed to the differences in mechanical performances, as my dogbones followed ISO standards (~1 mm thick), while the literature used ASTM standards (~4 mm). This hypothesis was validated experimentally, as increasing specimen thickness led to significant improvements in both Young's modulus (76.78±18.01 MPa) and tensile strength (8.20±0.04 MPa), bringing the values closer to those reported in the literature (orange curve).

In addition to testing hydrogels, I attempted tensile tests on bioplastic-state dogbones but was unsuccessful. Water is essential in softening the protein and PEG network and reducing the effective crosslink density, which compromises strength but enhances ductility, making hydrated samples more testable. In contrast, the absence of water in bioplastic-state samples led to warping and bending, preventing uniform load distribution during testing. This warping was often due to non-flat surfaces, which became more pronounced following treatment steps. To address this, I reverted to the original procedure but changed the dogbone fabrication method from casting to 3D printing, aiming for smoother surfaces and more reliable mechanical test results.

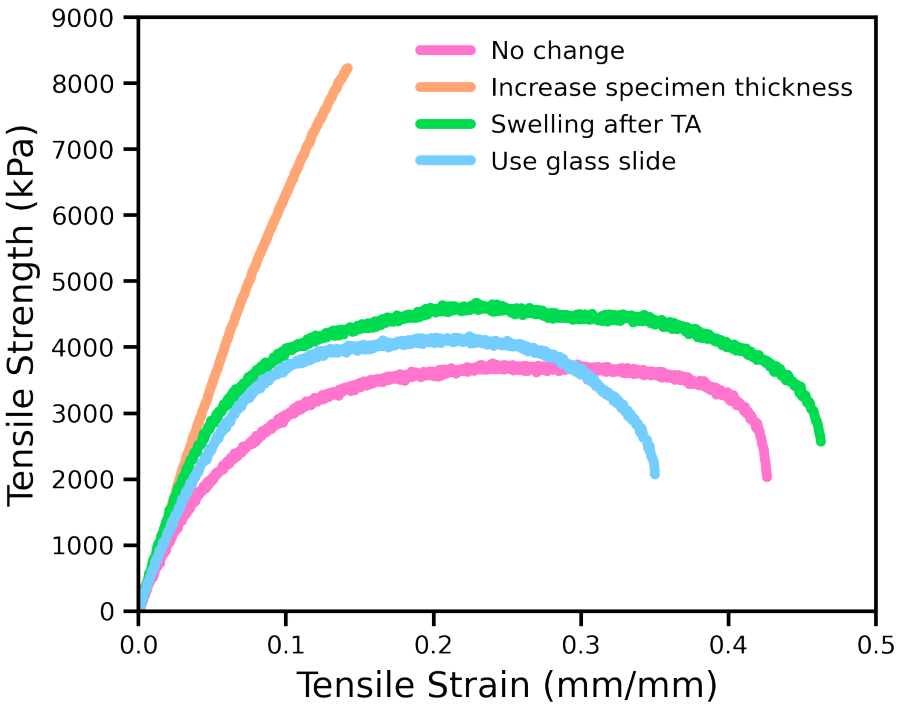

Figure 3.7. Representative tensile stress-strain curves of MA-BSA/2-HEA bioplastics after 24 hr swelling in DI water. Four different procedures were tested to optimize and reproduce the mechanical properties that have been reported.

By using DLP printing instead of traditional casting, a flatter surface was obtained to ensure proper layer formation. Even though this method introduced potential drawbacks, such as air bubbles becoming trapped within the printed structure due to the repeated motion of the printing head, it significantly reduced surface warping in the dogbone specimens. To further enhance printability, I began working with a resin formulation containing 30 wt% MA-BSA and 10 wt% PEG-DA, as the increased PEG-DA content has been shown to improve crosslinking density and printing fidelity. In Figure 3.8, mechanical testing revealed that both TA treatment and heat treatment had distinct effects on the material's performance, while the combination of the two showed a clear enhancement. Without any treatment, the MA-BSA/PEG-DA bioplastic material exhibited relatively poor mechanical properties, with a Young's modulus of 389.46

MPa, ultimate strength of 3.27 MPa, elongation of 0.81%, and toughness of 1.16 MJ/m^3. TA treatment alone doubled the toughness to 2.58 MJ/m^3 by significantly increasing both strength and elongation but keeping the modulus relatively the same, while heat treatment alone improved stiffness to 616.09 MPa and strength to 5.68 MPa but had minimal impact on ductility. Notably, the combination of TA and heat resulted in the best overall performance, with the highest values for Young's modulus (649.65 MPa), ultimate strength (15.50 MPa), and toughness (5.21 MJ/m^3), while maintaining elongation of 2.58%. With TA and heat treatment, the Young's modulus increased 2-fold, and ultimate tensile strength was improved 5-fold compared to no treatment samples. These results suggested that coating the bioplastic material with TA enhanced toughness through the formation of noncovalent interactions, particularly hydrogen bonding. Upon subsequent heating, the protein underwent denaturation and formed β-sheet structures, which significantly increase the material's stiffness, as shown in Young's modulus. The beta-sheet formation as protein's secondary structural change was also demonstrated by ATR-FTIR in Figure 3.9. When the absorbance peaks were normalized according to the maximum peak, the heat-induced denaturation of MA-BSA increased the intensity of a peak around 1622 cm^{-1} within the amide I region, which corresponding to the parallel beta-sheet formation.[52,58] This heating process also reduced the material's ability to rehydrate, which led to increased brittleness. When both TA and heat treatment were applied together, the material benefited from the effects of both processes and achieved improved toughness and stiffness simultaneously. This highlighted an effective strategy for optimizing the mechanical performance of bioplastics through combined chemical and thermal processing.

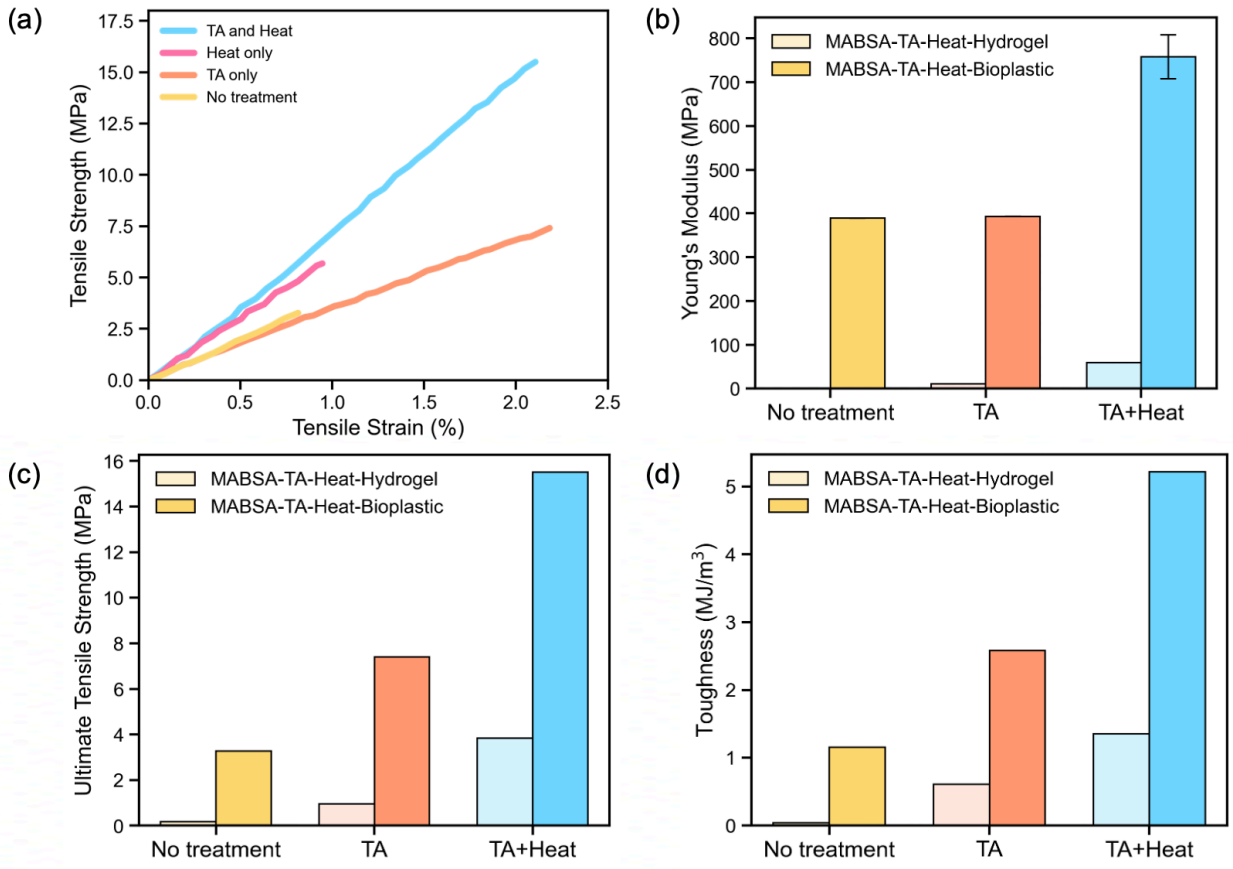

Figure 3.8. (a) Representative tensile stress-strain curves of MA-BSA/PEG-DA bioplastics with optimized processing methods as TA and heat treatments. Bar plots used to compare (b) Young's modulus (c) ultimate tensile strength, and (d) toughness between MA-BSA/PEG-DA hydrogels and bioplastics.

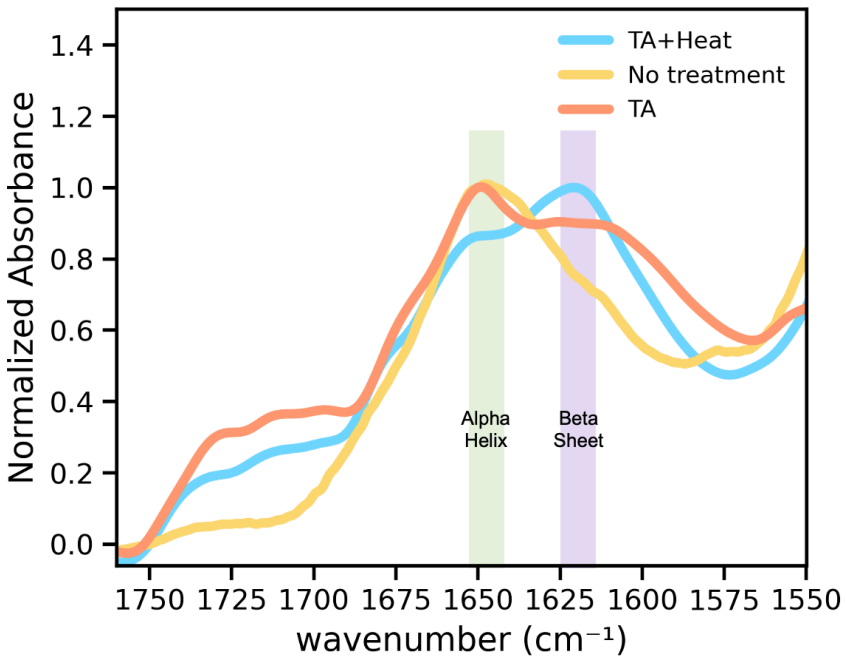

Figure 3.9. ATR-FTIR spectra of MA-BSA/PEG-DA with and without heat treatment. The beta-sheet peak formations are indicators of the heat-induced protein denaturation.

To better solve the problem brought up by uneven drying, a solvent exchange process was conducted. Solvent exchange has been largely applied to preserve the porosity and structures of hydrogels and assists rubbery-to-glassy transition of gels.[59–61] By soaking in 90% ethanol for 1 day right after print, the ethanol penetrated the MA-BSA/PEG-DA network and contributed to hold and bond both the hydrophobic and hydrophilic regions. After the additional solvent exchange, the non-treated MA-BSA/PEG-DA material showed a yield stress of 26.858±5.494 MPa with a Young's modulus of 500.835±53.326 MPa. With the help of solvent exchange and thermal annealing, the materials' ultimate strength doubled to 65.065±8.825 MPa and Young's modulus to 919.203±112.470 MPa. To further enhance the stiffness of the MA-BSA/PEG-DA bioplastics, the post-processing method as a combination of solvent exchange, TA and heat treatment afforded the highest modulus about 1385.968 ± 125.060 MPa as shown

in Figure 3.10 (b), thanks to the additional hydrogen bonds acted as sacrificial bonds to dissipate energy.

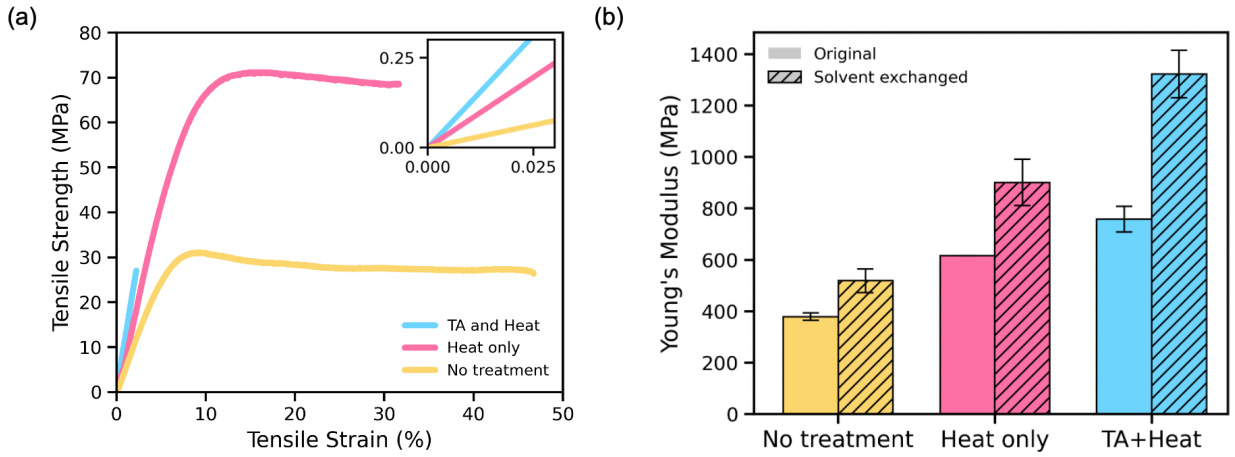

Figure 3.10. (a) Representative stress-strain curves of MA-BSA/PEG-DA bioplastics after solvent exchange and subsequent TA and/or heat treatment. (b) Bar plots used to compare the Young's modulus between MA-BSA/PEG-DA materials with and without solvent exchange.

By plotting the new mechanical data onto the Ashby plots, as illustrated in Figure 3.11, it becomes evident that the treatments involving tannic acid (TA), heat, and solvent exchange significantly contributed to enhancements in both material strength and stiffness. These optimized post-processing methods led to substantial improvements in mechanical performance, with both tensile strength and Young's modulus reaching the highest values recorded thus far for BSA-based bioplastics. Notably, these enhanced properties fill a previously unoccupied region on the Ashby plot, addressing the longstanding limitations of BSA-based materials in terms of mechanical robustness. As a result, these advancements not only validate the effectiveness of the processing strategies but also broaden the potential application scope of BSA-based materials, enabling their use in more demanding structural or functional contexts where higher strength and stiffness are required.

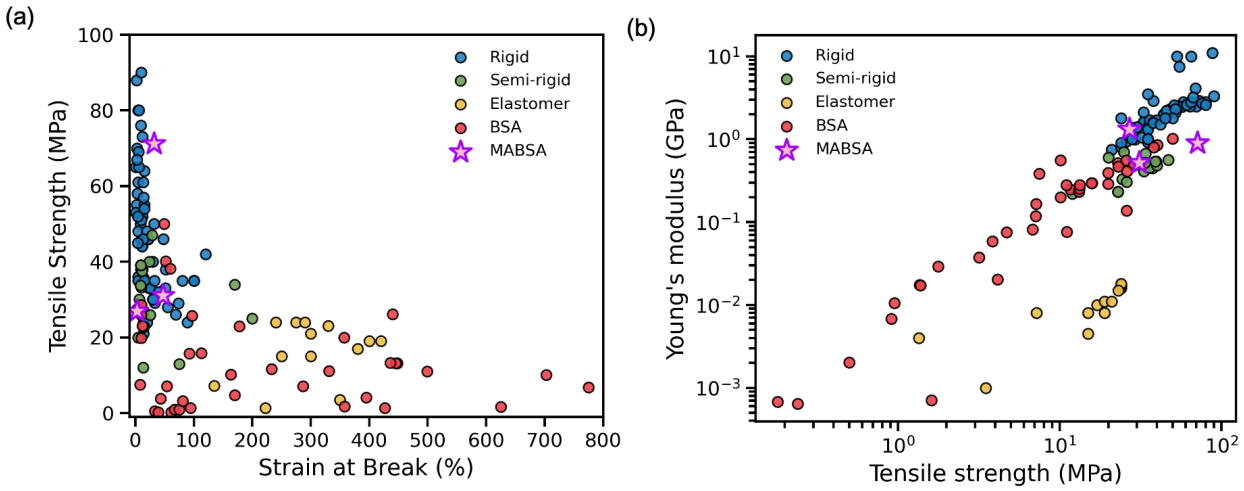

Figure 3.11. The new mechanical data of MA-BSA materials were plotted back to the Ashby plots with commercial resins. (a) Strain at break-tensile strength plot. (b) Tensile strength-Young's modulus plot.

3.2.5. Swelling Ratios

The swelling behaviors of MA-BSA bioplastics under different treatment conditions were evaluated by immersing in DI water. The untreated samples exhibited the highest swelling ratio, with an average of 142.17%. After treatment with TA alone, the swelling ratio significantly decreased to 66.32%, representing a reduction of approximately 2-fold compared to the untreated group. With the addition of heat treatment, the swelling ratio further decreased to 40.05%, corresponding to a 3.5-fold reduction. These results indicate that TA treatment has a notable reducing effect on the swelling ratio because of the increase of hydrogen bonding and thus creating a denser polymer network, while the combined thermal treatment to denature the protein component contributes to further network stabilization and suppression of water absorption. The findings in preventing rehydration open the doors for this protein-based bioplastics to find applications in practical fields.

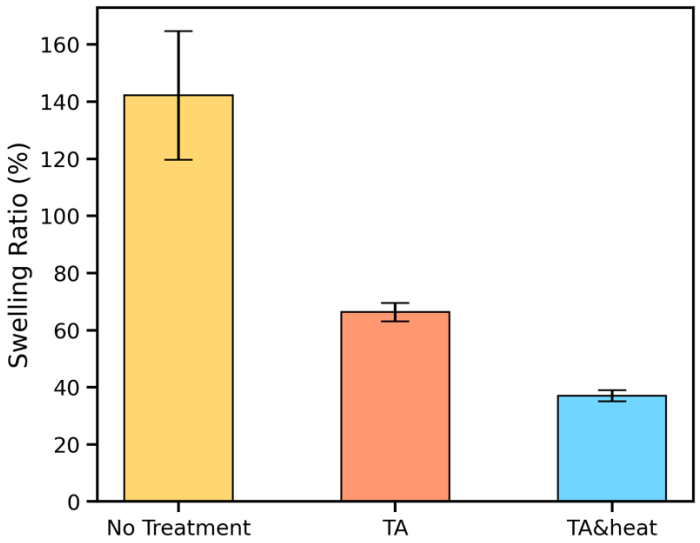

Figure 3.12. Bar plots showing the swelling ratio of MA-BSA/PEG-DA bioplastics (with no treatment, with TA treatment, and with both TA and heat treatment) after 72 hr swelling in DI water.

3.2.6. Future Work on Biocompatibility

To further evaluate the in vivo biocompatibility of MA-BSA-based bioplastics, an implantation study was conducted using 20 female C57BL/6 mice. The experiment was divided into four groups. Commercial polylactic acid (PLA) was used as the control material. Implantation outcomes are scheduled to be analyzed on days 14 and 28 post-implantation. Accordingly, 10 MA-BSA-based test samples and 10 PLA control samples were implanted. At day 14 and day 28, half of the animals (5 per group) will undergo blood collection and retrieval of the implanted discs along with the surrounding tissue. These samples will be used to assess subacute and subchronic toxicity responses, and the weights of the mice will be tracked. If results show low inflammation and acceptable systemic toxicity, MA-BSA-based bioplastics could be suitable for applications like tissue scaffolds, drug delivery, or implantable devices. Future works may

explore surface functionalization and compatibility with other printing platforms to expand its clinical potentials.

3.3. Conclusion

In conclusion, the mechanical properties of printable BSA-based bioplastics were compared with commercial resins using Ashby plots. The BSA/PEG network system showed tunable tensile strength and flexibility by formulating the composition of the network and its crosslinking chemistry. To further improve the mechanical profile of these protein bioplastics, 3D-printed MA-BSA/PEG-DA bioplastics were used as an example to undergo additional processing methods, such as TA swelling, heat treatment and solvent exchange method. The tensile results demonstrated a significant increase in Young's modulus and ultimate tensile strength compared to the non-treated materials. With the optimized processing methods, this study paved the way for biomedical applications of protein-based materials, offering a sustainable approach with desirable mechanical properties.

3.4. References

(1) Attaran, M. The Rise of 3-D Printing: The Advantages of Additive Manufacturing over Traditional Manufacturing. *Bus. Horiz.* **2017**, *60* (5), 677–688. https://doi.org/10.1016/j.bushor.2017.05.011.

(2) Pereira, T.; Kennedy, J. V.; Potgieter, J. A Comparison of Traditional Manufacturing vs Additive Manufacturing, the Best Method for the Job. *Procedia Manuf.* **2019**; Vol. 30, pp 11–18. https://doi.org/10.1016/j.promfg.2019.02.003.

(3) Najmon, J. C.; Raeisi, S.; Tovar, A. Review of Additive Manufacturing Technologies and Applications in the Aerospace Industry. *Additive Manufacturing for the Aerospace Industry* **2019**, 7–31. https://doi.org/10.1016/B978-0-12-814062-8.00002-9.

(4) Blakey-Milner, B.; Gradl, P.; Snedden, G.; Brooks, M.; Pitot, J.; Lopez, E.; Leary, M.; Berto, F.; du Plessis, A. Metal Additive Manufacturing in Aerospace: A Review. *Mater Des.* **2021**, *209*. https://doi.org/10.1016/j.matdes.2021.110008.

(5) Vasco, J. C. Additive Manufacturing for the Automotive Industry. *Additive Manufacturing* **2021**; pp 505–530. https://doi.org/10.1016/B978-0-12-818411-0.00010-0.

(6) Böckin, D.; Tillman, A. M. Environmental Assessment of Additive Manufacturing in the Automotive Industry. *J. Clean. Prod.* **2019**, *226*, 977–987. https://doi.org/10.1016/j.jclepro.2019.04.086.

(7) Lim, C. W. J.; Le, K. Q.; Lu, Q.; Wong, C. H. An Overview of 3-D Printing in Manufacturing, Aerospace, and Automotive Industries. *IEEE Potentials* **2016**, *35* (4), 18–22. https://doi.org/10.1109/MPOT.2016.2540098.

(8) Zadpoor, A. A.; Malda, J. Additive Manufacturing of Biomaterials, Tissues, and Organs. *Annals of Biomedical Engineering* **2017**. https://doi.org/10.1007/s10439-016-1719-y.

(9) Rezvani Ghomi, E.; Khosravi, F.; Neisiany, R. E.; Singh, S.; Ramakrishna, S. Future of Additive Manufacturing in Healthcare. *Curr. Opin. Biomed. Eng.* **2021**. https://doi.org/10.1016/j.cobme.2020.100255.

(10) Bhargav, A.; Sanjairaj, V.; Rosa, V.; Feng, L. W.; Fuh YH, J. Applications of Additive Manufacturing in Dentistry: A Review. *J. Biomed. Mater. Res.* **2018**, pp 2058–2064. https://doi.org/10.1002/jbm.b.33961.

(11) Zhu, Y.; Guo, S.; Ravichandran, D.; Ramanathan, A.; Sobczak, M. T.; Sacco, A. F.; Patil, D.; Thummalapalli, S. V.; Pulido, T. V.; Lancaster, J. N.; Yi, J.; Cornella, J. L.; Lott, D. G.; Chen, X.; Mei, X.; Zhang, Y. S.; Wang, L.; Wang, X.; Zhao, Y.; Hassan, M. K.; Chambers, L. B.; Theobald, T. G.; Yang, S.; Liang, L.; Song, K. 3D-Printed Polymeric Biomaterials for Health Applications. *Advanced Healthcare Materials* **2024**. https://doi.org/10.1002/adhm.202402571.

(12) Yap, Y. L.; Yeong, W. Y. Additive Manufacture of Fashion and Jewellery Products: A Mini Review: This Paper Provides an Insight into the Future of 3D Printing Industries for Fashion and Jewellery Products. *Virtual Phys. Prototyp.* **2014**, *9* (3), 195–201. https://doi.org/10.1080/17452759.2014.938993.

(13) Javaid, M.; Haleem, A. Current Status and Applications of Additive Manufacturing in Dentistry: A Literature-Based Review. *J. Oral Biol. Craniofacial Res.* **2019**, pp 179–185. https://doi.org/10.1016/j.jobcr.2019.04.004.

(14) Kessler, A.; Hickel, R.; Reymus, M. 3D Printing in Dentistry-State of the Art. *Oper. Dent.* **2020**, *45* (1), 30–40. https://doi.org/10.2341/18-229-L.

(15) Ligon, S. C.; Liska, R.; Stampfl, J.; Gurr, M.; Mülhaupt, R. Polymers for 3D Printing and Customized Additive Manufacturing. *Chemical Reviews* **2017**, pp 10212–10290. https://doi.org/10.1021/acs.chemrev.7b00074.

(16) Calignano, F.; Manfredi, D.; Ambrosio, E. P.; Biamino, S.; Lombardi, M.; Atzeni, E.; Salmi, A.; Minetola, P.; Iuliano, L.; Fino, P. Overview on Additive Manufacturing Technologies. *Proceedings of the IEEE* **2017**, *105* (4), 593–612. https://doi.org/10.1109/JPROC.2016.2625098.

(17) Bagheri, A.; Jin, J. Photopolymerization in 3D Printing. *ACS Applied Polymer Materials* **2019**, pp 593–611. https://doi.org/10.1021/acsapm.8b00165.

(18) Zhang, F.; Zhu, L.; Li, Z.; Wang, S.; Shi, J.; Tang, W.; Li, N.; Yang, J. The Recent Development of Vat Photopolymerization: A Review. *Additive Manufacturing* **2021**. https://doi.org/10.1016/j.addma.2021.102423.

(19) Hull, C. W. Apparatus for Production of Three-dimensional Objects by Stereothography. US4575330A, 1986.

(20) Gross, B. C.; Erkal, J. L.; Lockwood, S. Y.; Chen, C.; Spence, D. M. Evaluation of 3D Printing and Its Potential Impact on Biotechnology and the Chemical Sciences. *Anal. Chem.* **2014**, *86* (7), 3240–3253. https://doi.org/10.1021/ac403397r.

(21) Florence, J. M.; Yoder, L. A. Display System Architectures for Digital Micromirror Device (DMD)-Based Projectors. **1996**, *2650*. https://doi.org/10.1117/12.237004.

(22) Subedi, S.; Liu, S.; Wang, W.; Naser Shovon, S. M. A.; Chen, X.; Ware, H. O. T. Multi-Material Vat Photopolymerization 3D Printing: A Review of Mechanisms and Applications. *Advanced Manufacturing* **2024**, *1* (1), 9. https://doi.org/10.1038/s44334-024-00005-w.

(23) Chaudhary, R.; Fabbri, P.; Leoni, E.; Mazzanti, F.; Akbari, R.; Antonini, C. Additive Manufacturing by Digital Light Processing: A Review. *Progress in Additive Manufacturing* **2023**, pp 331–351. https://doi.org/10.1007/s40964-022-00336-0.

(24) Mondschein, R. J.; Kanitkar, A.; Williams, C. B.; Verbridge, S. S.; Long, T. E. Polymer Structure-Property Requirements for Stereolithographic 3D Printing of Soft Tissue Engineering Scaffolds. *Biomaterials* **2017**, pp 170–188. https://doi.org/10.1016/j.biomaterials.2017.06.005.

(25) Appuhamillage, G. A.; Chartrain, N.; Meenakshisundaram, V.; Feller, K. D.; Williams, C. B.; Long, T. E. 110th Anniversary: Vat Photopolymerization-Based Additive Manufacturing: Current Trends and Future Directions in Materials Design. *Industrial and Engineering Chemistry Research* **2019**, pp 15109–15118. https://doi.org/10.1021/acs.iecr.9b02679.

(26) Stubbins, A.; Law, K. L.; Muñoz, S. E.; Bianchi, T. S.; Zhu, L. Plastics in the Earth System. *Science* **2021**, *373*, 51–55.

(27) Singh, N.; Walker, T. R. Plastic Recycling: A Panacea or Environmental Pollution Problem. *Materials Sustainability* **2024**, *2* (1). https://doi.org/10.1038/s44296-024-00024-w.

(28) Cole, M.; Lindeque, P.; Halsband, C.; Galloway, T. S. Microplastics as Contaminants in the Marine Environment: A Review. *Mar. Pollut. Bull.* **2011**, pp 2588–2597. https://doi.org/10.1016/j.marpolbul.2011.09.025.

(29) Nihart, A. J.; Garcia, M. A.; El Hayek, E.; Liu, R.; Olewine, M.; Kingston, J. D.; Castillo, E. F.; Gullapalli, R. R.; Howard, T.; Bleske, B.; Scott, J.; Gonzalez-Estrella, J.; Gross, J. M.; Spilde, M.; Adolphi, N. L.; Gallego, D. F.; Jarrell, H. S.; Dvorscak, G.; Zuluaga-Ruiz, M. E.; West, A. B.; Campen, M. J. Bioaccumulation of Microplastics in Decedent Human Brains. *Nat. Med.* **2025**. https://doi.org/10.1038/s41591-024-03453-1.

(30) Stanley, J.; Culliton, D.; Jovani-Sancho, A. J.; Neves, A. C. The Journey of Plastics: Historical Development, Environmental Challenges, and the Emergence of Bioplastics for Single-Use Products. *Eng.* **2025**, *6* (1). https://doi.org/10.3390/eng6010017.

(31) Ali, S. S.; Abdelkarim, E. A.; Elsamahy, T.; Al-Tohamy, R.; Li, F.; Kornaros, M.; Zuorro, A.; Zhu, D.; Sun, J. Bioplastic Production in Terms of Life Cycle Assessment: A State-of-the-Art Review. *Environmental Science and Ecotechnology* **2023**. https://doi.org/10.1016/j.ese.2023.100254.

(32) Zhao, P.; Rao, C.; Gu, F.; Sharmin, N.; Fu, J. Close-Looped Recycling of Polylactic Acid Used in 3D Printing: An Experimental Investigation and Life Cycle Assessment. *J. Clean. Prod.* **2018**, *197*, 1046–1055. https://doi.org/10.1016/j.jclepro.2018.06.275.

(33) Melchels, F. P. W.; Velders, A. H.; Feijen, J.; Grijpma, D. W. Photo-Cross-Linked Poly(Dl -Lactide)-Based Networks. Structural Characterization by HR-MAS NMR Spectroscopy

and Hydrolytic Degradation Behavior. *Macromolecules* **2010**, *43* (20), 8570–8579. https://doi.org/10.1021/ma1011705.

(34) Tan, S. G.; Chow, W. S. Curing Characteristics and Thermal Properties of Epoxidized Soybean Oil Based Thermosetting Resin. *J. Am. Oil Chem. Soc.* **2011**, *88* (7), 915–923. https://doi.org/10.1007/s11746-010-1748-x.

(35) Habib, F.; Bajpai, M. Chemistry Synthesis and Characterization of Acrylated Epoxidized Soybean Oil for UV Cured Coatings. *Chemistry & Chemical Technology* **2011**, *5* (3).

(36) Elsawy, M. A.; Kim, K. H.; Park, J. W.; Deep, A. Hydrolytic Degradation of Polylactic Acid (PLA) and Its Composites. *Renewable and Sustainable Energy Reviews* **2017**, pp 1346–1352. https://doi.org/10.1016/j.rser.2017.05.143.

(37) Andanje, M. N.; Mwangi, J. W.; Mose, B. R.; Carrara, S. Biocompatible and Biodegradable 3D Printing from Bioplastics: A Review. *Polymers* **2023**. https://doi.org/10.3390/polym15102355.

(38) Van Den Bulcke, A. I.; Bogdanov, B.; De Rooze, N.; Schacht, E. H.; Cornelissen, M.; Berghmans, H. Structural and Rheological Properties of Methacrylamide Modified Gelatin Hydrogels. *Biomacromolecules* **2000**, *1* (1), 31–38. https://doi.org/10.1021/bm990017d.

(39) Zhu, M.; Wang, Y.; Ferracci, G.; Zheng, J.; Cho, N. J.; Lee, B. H. Gelatin Methacryloyl and Its Hydrogels with an Exceptional Degree of Controllability and Batch-to-Batch Consistency. *Sci. Rep.* **2019**, *9* (1). https://doi.org/10.1038/s41598-019-42186-x.

(40) Klotz, B. J.; Gawlitta, D.; Rosenberg, A. J. W. P.; Malda, J.; Melchels, F. P. W. Gelatin-Methacryloyl Hydrogels: Towards Biofabrication-Based Tissue Repair. *Trends in Biotechnology* **2016**, pp 394–407. https://doi.org/10.1016/j.tibtech.2016.01.002.

(41) Kumar, H.; Sakthivel, K.; Mohamed, M. G. A.; Boras, E.; Shin, S. R.; Kim, K. Designing Gelatin Methacryloyl (GelMA)-Based Bioinks for Visible Light Stereolithographic 3D Biofabrication. *Macromo.l Biosci.* **2021**, *21* (1). https://doi.org/10.1002/mabi.202000317.

(42) Xiong, X.; Qing, Q.; Cheng, S.; Yuan, R.; Yang, D.; Wei, G.; Jing, T.; Li, Z.; Qu, S. Gelatin Methacryloyl-Adsorbed Calcium Phosphate Nanoparticles for 3D Printing of Bone Repair Scaffolds via Digital Light Processing. *ACS Appl Nano Mater* **2025**. https://doi.org/10.1021/acsanm.5c00400.

(43) Kim, S. H.; Yeon, Y. K.; Lee, J. M.; Chao, J. R.; Lee, Y. J.; Seo, Y. B.; Sultan, M. T.; Lee, O. J.; Lee, J. S.; Yoon, S. Il; Hong, I. S.; Khang, G.; Lee, S. J.; Yoo, J. J.; Park, C. H. Precisely Printable and Biocompatible Silk Fibroin Bioink for Digital Light Processing 3D Printing. *Nat. Commun.* **2018**, *9* (1). https://doi.org/10.1038/s41467-018-03759-y.

(44) Hong, H.; Seo, Y. B.; Kim, D. Y.; Lee, J. S.; Lee, Y. J.; Lee, H.; Ajiteru, O.; Sultan, M. T.; Lee, O. J.; Kim, S. H.; Park, C. H. Digital Light Processing 3D Printed Silk Fibroin Hydrogel for Cartilage Tissue Engineering. *Biomaterials* **2020**, *232*. https://doi.org/10.1016/j.biomaterials.2019.119679.

(45) *3D Printing Trend Report 2024*. Protolabs.com. https://www.protolabs.com/resources/guides-and-trend-reports/3d-printing-trend-report/#marketgrowth (accessed 2025-04-24)

(46) *Plastics-Determination of Tensile Properties*; 2012. www.iso.org.

(47) Jahan, A.; Ismail, M. Y.; Sapuan, S. M.; Mustapha, F. Material Screening and Choosing Methods - A Review. *Mater. Des.* **2010**, *31* (2), 696–705. https://doi.org/10.1016/j.matdes.2009.08.013.

(48) Shah, D. U. Natural Fibre Composites: Comprehensive Ashby-Type Materials Selection Charts. *Mater. Des.* **2014**, *62*, 21–31. https://doi.org/10.1016/j.matdes.2014.05.002.

(49) Asmare Fentahun, M.; Ahsen Savaş, M. Materials Used in Automotive Manufacture and Material Selection Using Ashby Charts. *International Journal of Materials Engineering* **2018**, *8* (3), 40–54. https://doi.org/10.5923/j.ijme.20180803.02.

(50) Smith, P. T.; Narupai, B.; Tsui, J. H.; Millik, S. C.; Shafranek, R. T.; Kim, D. H.; Nelson, A. Additive Manufacturing of Bovine Serum Albumin-Based Hydrogels and Bioplastics. *Biomacromolecules* **2020**, *21* (2), 484–492. https://doi.org/10.1021/acs.biomac.9b01236.

(51) Smith, P. T.; Altin, G.; Millik, S. C.; Narupai, B.; Sietz, C.; Park, J. O.; Nelson, A. Methacrylated Bovine Serum Albumin and Tannic Acid Composite Materials for Three-Dimensional Printing Tough and Mechanically Functional Parts. *ACS Appl. Mater. Interfaces.* **2022**, *14* (18), 21418–21425. https://doi.org/10.1021/acsami.2c01446.

(52) Sanchez-Rexach, E.; Smith, P. T.; Gomez-Lopez, A.; Fernandez, M.; Cortajarena, A. L.; Sardon, H.; Nelson, A. 3D-Printed Bioplastics with Shape-Memory Behavior Based on Native Bovine Serum Albumin. *ACS Appl. Mater. Interfaces.* **2021**, *13* (16), 19193–19199. https://doi.org/10.1021/acsami.0c22377.

(53) Millik, S. C.; Sadaba, N.; Hilburg, S. L.; Sanchez-Rexach, E.; Zhang, M.; Yu, S.; Vass, A. F.; Pozzo, L. D.; Nelson, A. 3D-Printed Protein-Based Bioplastics with Tunable Mechanical Properties Using Glycerol or Hyperbranched Poly(Glycerol)s as Plasticizers. *Biomacromolecules* **2025**. https://doi.org/10.1021/acs.biomac.4c01497.

(54) Tibbitt, M. W.; Kloxin, A. M.; Sawicki, L. A.; Anseth, K. S. Mechanical Properties and Degradation of Chain and Step-Polymerized Photodegradable Hydrogels. *Macromolecules* **2013**, *46* (7), 2785–2792. https://doi.org/10.1021/ma302522x.

(55) Lin, C. C.; Raza, A.; Shih, H. PEG Hydrogels Formed by Thiol-Ene Photo-Click Chemistry and Their Effect on the Formation and Recovery of Insulin-Secreting Cell Spheroids. *Biomaterials* **2011**, *32* (36), 9685–9695. https://doi.org/10.1016/j.biomaterials.2011.08.083.

(56) Chen, C.; Yang, H.; Yang, X.; Ma, Q. Tannic Acid: A Crosslinker Leading to Versatile Functional Polymeric Networks: A Review. *RSC Adv.* **2022**, pp 7689–7711. https://doi.org/10.1039/d1ra07657d.

(57) Mercadal, P. A.; Martínez, Y. M.; Zoratti, M.; Velasco, M. I.; Romero, M. R.; Tommasone, G.; Picchio, M. L.; González, A. Tannic Acid-Enhanced Gelatin Double Network Eutectogels Using Polymerizable Eutectic Solvents. *ACS Appl. Polym. Mater.* **2025**. https://doi.org/10.1021/acsapm.4c03081.

(58) Militello, V.; Casarino, C.; Emanuele, A.; Giostra, A.; Pullara, F.; Leone, M. Aggregation Kinetics of Bovine Serum Albumin Studied by FTIR Spectroscopy and Light Scattering. *Biophys. Chem.* **2004**, *107* (2), 175–187. https://doi.org/10.1016/j.bpc.2003.09.004.

(59) Gurikov, P.; S. P., R.; Griffin, J. S.; Steiner, S. A.; Smirnova, I. 110th Anniversary: Solvent Exchange in the Processing of Biopolymer Aerogels: Current Status and Open Questions. *Ind. Eng. Chem. Res.* **2019**, *58* (40), 18590–18600. https://doi.org/10.1021/acs.iecr.9b02967.

(60) Hu, J. Y.; Hou, L. X.; Zhu, A.; Qiu, H. N.; Zhang, Z. R.; Du, C.; Cui, K.; Zheng, Q.; Wu, Z. L. Solvent Exchange-Induced Microphase Separation and Structural Arrest to Form Glassy Hydrogels. *Macromolecules* **2024**. https://doi.org/10.1021/acs.macromol.4c01758.

(61) Duereh, A.; Guo, H.; Honma, T.; Hiraga, Y.; Sato, Y.; Lee Smith, R.; Inomata, H. Solvent Polarity of Cyclic Ketone (Cyclopentanone, Cyclohexanone): Alcohol (Methanol, Ethanol) Renewable Mixed-Solvent Systems for Applications in Pharmaceutical and Chemical Processing. *Ind. Eng. Chem. Res.* **2018**, *57* (22), 7331–7344. https://doi.org/10.1021/acs.iecr.8b00689.